Nordic nuclear safety research

NKS-394
ISBN 978-87-7893-482-6

Modelling as a Tool to Augment Ground Motion Data in Regions of Diffuse Seismicity – Final report

Ludovic Fülöp[1]
Vilho Jussila[1]
Björn Lund[2]
Billy Fälth[2]
Peter Voss[3]
Jari Puttonen[4]
Jouni Saari[5]
Pekka Heikkinen[6]

[1]VTT Technical research Centre in Finland Oy
[2]Uppsala University, Sweden
[3]Geological Survey of Denmark and Greenland
[4]Aalto University, Finland
[5]ÅF Consult Oy, Finland
[6]Institute of Seismology, University of Helsinki, Finland

August 2017

Abstract

De-aggregation of probabilistic hazard assessment (PSHA) results show that the dominating source of vibrations with engineering significance to NPP safety is from mid-magnitude earthquakes located at close distances to the plant. This region is called the “near-field” and is known for its particularities when compared to “far-field”. For example, significant duration of the ground motions is shorter, corresponding to S-wave and surface wave arrivals; there are distinctive high velocity peaks in the ground motions and vertical shaking components may exceed horizontal components. These particularities are known to have design consequences, but are often overlooked by engineering codes.
In Fennoscandia, near-field observations of larger magnitude (M>3) earthquakes are missing, and modelling is the only way to supplement the existing empirical data underspinning the attenuation equations in the PSHA studies.
During the project year 2015, we confirmed the near-source effect in small magnitude earthquake recordings in Finland and developed modeling skills and tools to generate synthetic, near-field accelerograms starting from process of the fault rupture.
Within this report (2016), we describe the modelling techniques and compare the modelling outcomes for Mw=5.5 earthequakes with ground motion prediction equations GMPE’s developed for stable continental regions. Five cases were analyzed in order to explore the capabilities of ground motion simulation tools. In the five cases, the varied parameters were depth of the source, dip angle of the fault and dynamic properties of the fault. The models were developed in COMPSYN in 3DEC.
By these comparisons we highlight the potentials and limitations of modelling to support empirical observations.

Key words

Nuclear power plant safety, earthquake, near-field effects, fault source modeling

NKS-394
ISBN 978-87-7893-481-9
Electronic report, August 2017
NKS Secretariat
P.O. Box 49
DK - 4000 Roskilde, Denmark
Phone +45 4677 4041
www.nks.org
e-mail nks@nks.org

MODELLING AS A TOOL TO AUGMENT GROUND MOTION DATA IN REGIONS OF DIFFUSE SEISMICITY – Final report

Final Report from ADdGROUND Contract: NKS-R(16)113/1

Ludovic Fülöp[1], Vilho Jussila[1]

Björn Lund[2], Billy Fälth[2]

Peter Voss[3]

Jari Puttonen[4]

Jouni Saari[5]

Pekka Heikkinen[6]

[1] VTT Technical research Centre in Finland Oy

[2] Uppsala University

[3] Geological Survey of Denmark and Greenland

[4] Aalto University

[5] ÅF Consult Oy

[6] Institute of Seismology, University of Helsinki

Table of contents

Abbreviations

EMP-GMPE	– ground motion prediction equation by Vuorinen (2015), called “*the empirical model*” in the original publication
FF	– far-field
GMPE	– ground motion prediction equation
GM	– geometric mean
G16	– ground motion prediction equation by Graizer (2016)
NF	– near-field
NF-GMPE	– new Fennoscandian GMPEs by Vuorinen (2015), called “*the referenced empirical model*” in the original publication
NKS	– Nordic Nuclear Safety Research
NPP	– nuclear power plant
PGA	– peak ground acceleration
PSA	– pseudo-acceleration spectra
REF-GMPE	– ground motion prediction equation by Vuorinen (2015)
RotD50	– direction independent horizontal component PSA (Boore et al., 2006), 50 stands for 50% probability of non-exceedance
RotD100	– direction independent horizontal component PSA (Boore et al., 2006), 100 stands for 100% probability (i.e. absolute certainty) of non-exceedance
SA_f	– spectral acceleration at the frequency
SA_{10Hz}	– spectral acceleration at 10Hz
SA_{4Hz}	– spectral acceleration at 4Hz
US	– United States
YVL	– Ydinturvallisuusohjeet (Finnish Regulatory Guides on Nuclear Safety)

1 Introduction

1.1 Background

This report is a continuation of the progress reported by the same project for the year 2015 (Fülöp et al., 2016). Within that progress report we highlighted some aspects related to the characteristics and possible effect of near-field earthquakes. We also emphasised how these types of earthquakes may influence the design of nuclear power plant (NPP) installations. At the end of the progress report we introduced concepts and techniques of source modelling, which we planned to develop and exploit in year 2016 of the project.

Within this report, we describe the modelling techniques explored in 2016 and compare the modelling outcomes with ground motion prediction equations (GMPEs) developed for stable continental regions. However, the comparisons with the new Fennoscandian GMPEs were disregarded due to the issues highlighted in Section 4.5 of this report "*Analysis of the GMPEs with regard to spectral shape and criticism of the new Fennoscandia GMPE*". By these comparisons we highlight the potentials and limitations of modelling to support empirical observations.

The general outcome of this NKS work is that we demonstrate the modelling techniques for a limited number of earthquake scenarios. The deployment of such modelling to support the safety case of NPPs was out of scope of this NKS project, but we hope that this project gives a basis for further development and later deployment.

1.2 Seismicity of Fennoscandia

Before advancing to the description of the work carried out here, we present a short highlight of the seismicity in Fennoscandia, and of the research direction sketched in 2015 by this research group:

- Magnitude distance de-aggregation from of the earthquake hazard for certain locations in Finland was carried out by Malm and Saari, (2014). The de-aggregation for Pyhäjoki of the 5 % damping average horizontal component peak-ground acceleration (PGA) and 4 Hz and 10 Hz spectral acceleration (SA) shows strong contributions as follows
    - PGA=0.05×g, magnitude M=4.1 and distance D=29km,
    - PGA=0.1×g, magnitude M=4.3 and distance D=24km,
    - PGA=0.2×g, magnitude M=4.4 and distance D=21km;
    - SA_{4Hz}=0.05×g magnitude M=3.8 and distance D=34km;
    - SA_{4Hz}=0.1×g magnitude M=3.6 and distance D=22km;
    - SA_{4Hz}=0.2×g magnitude M=3.2 and distance D=11km;
    - SA_{10Hz}=0.1×g magnitude M=4.3 and distance D=40km;
    - SA_{10Hz}=0.2×g magnitude M=4.4 and distance D=33km;
    - SA_{10Hz}=0.4×g magnitude M=4.4 and distance D=26km;

  If we approximate that ~4 Hz correspond to the natural frequency of the rigid reactor structure and ~10 Hz is relevant for the vibration frequencies of floors in the vertical direction and equipment and considering the distribution of probability densities, we can state that most hazard to the NPPs and equipment come from distances within <60 km. This conclusion is consistent with finding from other regions of moderate seismicity (SWISSNUCLEAR, 2004a).

- The GMPEs developed using empirical data normally rely on very few recordings in this range of distances. In the progress report of AddGROUND we pointed out that the new Fennoscandian GMPEs (Vuorinen, 2015) are practically calibrated by very few data points for M>4 and D<100 km (Figure 1);

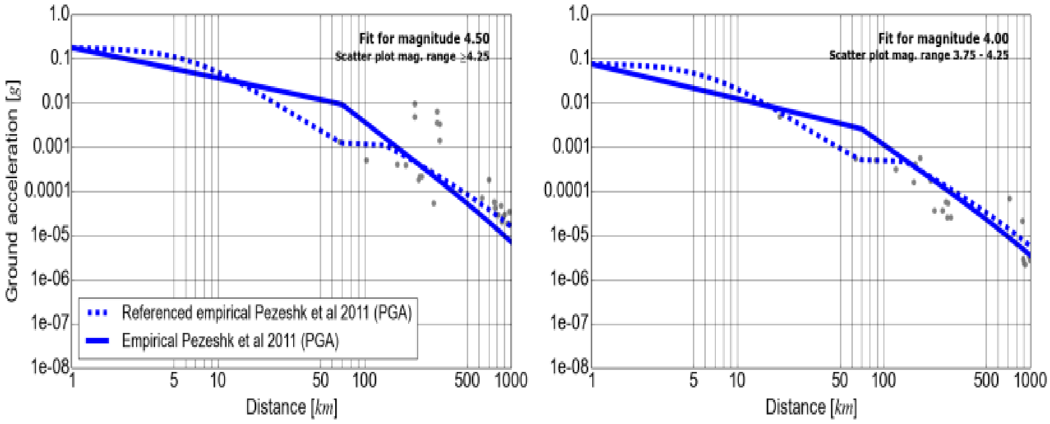

Figure 1. PGA of the recordings from Fennoscandia used for the calibration of the new Fennoscandian GMPEs in the M>4 magnitude range. (a) Shows the all data points from magnitude M≥4.25, while (b) from the bin 3.75≤M<4.25 (Vuorinen, 2015). Continuous blue line is the empirical ground motion prediction equation (EMP-GMPE) and dashed blue line is the reference empirical GMPE (REF-GMPE) calibrated to the Fennoscandian data. The two GMPEs are called generically new Fennoscandian GMPEs in this report.

- The design spectra proposed in the YVL guide in Finland (red-line line in Figure 2) reassembles near-field (NF) earthquakes (bold black line in Figure 2). In the YVL spectra, the amplification at 3-4Hz is about 1.3×PGA while it is <1 for NF and >2 for far-field (FF). The YVL spectra peaks at 10Hz, while the FF spectra at 7.5Hz and the NF spectra in the range of 12-18Hz.

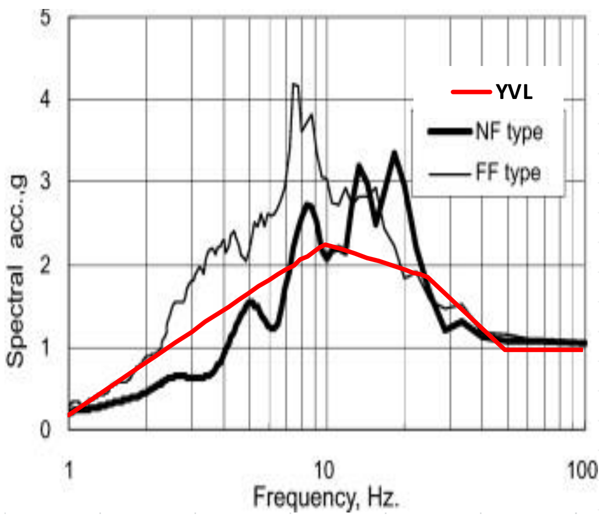

Figure 2. Normalized shape of design spectra in the YVL guide with red line (YVL B.7, 2013), developed primarily for southern Finland and normalized pseudo-acceleration (PSA) spectra of near-field (NF) and far-field (FF) type shaking (Labbé and Altinyollar, 2011).

- When it comes to the potential damaging effects of high frequency waves, there is a consensus in the technical literature that the main concern is not structures (Labbé and Altinyollar, 2011). No structures were damaged by earthquakes with very high PGAs generated by high-frequency content. However, features of such earthquakes need to be considered when computing floor spectra and qualifying components of NPPs.
- The effects of earthquakes in the near-field (in the engineering sense), are well known. As one comes closer to the epicentre of the earthquake, shorter durations, larger velocity peaks and more directivity of the ground motion can be expected. The balance between horizontal and vertical ground motion can also change (Figure 3).

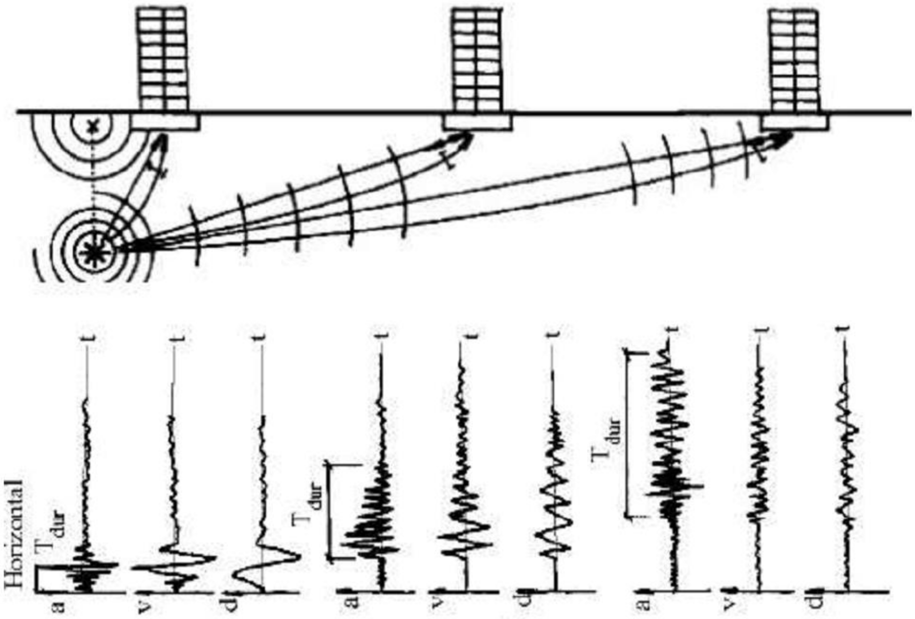

Figure 3. General effect of distance (increasing from left to right) on the observed shaking as accelerations (a), velocities (v) and displacement (d) (Gioncu and Mazzolani, 2011)

1.3 Objectives of the study

The objective of the study was to estimate the viability of GMPEs, generally thought suitable for use in Fennoscandia, with regards to their prediction in the vicinity of the fault. The distance of interest was <50km, magnitudes in the higher range of values used in hazard predictions ($4<M_w<6$) and ground properties corresponding to very hard-rock (V_{s30}>2000 km/s).

On the long term, the aim is to provide proposals for more accurate ground motion predictions in the near-field. Obviously, in order to achieve this goal the number of modelled earthquake scenarios has to be larger. Hence, only preliminary suggestions can be given with regards to this objective.

In the first section, we introduce the proposed modelling technique and justify the fault rupture scenarios used.

Then, we present the technique used for modelling the rupture process of the fault. For larger earthquakes, the fault size can be several kilometres to hundreds of kilometres. Once the stress equilibrium is overcome at a particular location (hypocentre), the rupture of the fault initiates and propagates along the fault until the kinetic energy is dissipated. Finite difference based dynamic modelling was used to simulate this rupture process.

In the third section we describe the modelling of the propagation of vibrations. It is not feasible to model the propagation with the same numerical methodology as that used for the fault rupture simulation. Thus, for the wave propagation modelling we use kinematic models instead. The complementary use of the two methods is called hybrid modelling in this report.

In the fourth section we discuss the possible measurement data with which we could compare the modelling results. Due to the considerable complexity and randomness of both the fault rupture process and of the wave propagation, it is not so relevant to compare the result of a generic simulation to the recordings from individual events. Additionally, there are no near-field measurements from events observed in Fennoscandia of the magnitude we model. Hence, our primary comparisons are to ground motion prediction equations (GMPEs), which synthetize the expected ground motion based on observations. Two such GMPEs are described: the new Fennoscandian GMPEs already mentioned in the introduction, and G16 proposed for the central US by Graizer (2016).

In the final sections of the report we present some model outputs, make comparisons of the modelling output to the G16 and highlight the potential of the proposed modelling technique.

2 Modelling approach

To build and run a numerical model which simulates a dynamic fault rupture as well as the propagation of the generated high frequency waves (e.g. > 5 Hz) to distances tens of kilometres from the fault is extremely computationally demanding. Such a model would need many tens of millions of elements for the discretization of the continuum and requires supercomputer capabilities to handle, especially if one wants to study several earthquake rupture scenarios. Thus, we apply a hybrid modelling approach inspired by the tests performed in Fälth et al. (2015). The approach comprises two steps:

1. An earthquake source model is generated using dynamic rupture modelling. The dynamic rupture is modelled using the 3DEC software package (Itasca, 2013). The model comprises a fault plane embedded in a finely discretized small rock volume. The dimensions of the model are set just large enough to prevent the boundaries from influencing the solution. The simulation time needs to be long enough for the rupture and slip development to be completed over the entire fault plane. An initial stress field is applied and a dynamic earthquake rupture is initiated and propagated along the fault plane. The fault slip temporal evolution is recorded at a large number of points on the fault.
2. The slip function parameter values determined in the previous step are used as input to the kinematic earthquake modelling software Compsyn (Spudich and Xu, 2003). Compsyn is a discrete wavenumber/finite element program for solving the wave equation in models with horizontal layers. The numerical approach adopted by Compsyn differs considerably from that of 3DEC and it is much more efficient for ground motion calculations, given that a fault rupture model is available.

Since the objective of this work was primarily to demonstrate the modelling approach, we restricted the work to a few earthquake scenarios which can be regarded as representative for earthquakes occurring within the Baltic Shield. The moment magnitude of the simulated earthquakes is $M_w = 5.5$, which corresponds approximately to the magnitudes of the largest historic events in the region. According to the data base regressions by Leonard (2010) this magnitude corresponds approximately to a 25 km^2 rupture area. It was schematically assumed that the rupture area is square-shaped with edge length 5 km. Many earthquakes in the Baltic shield take place at mid-crustal levels (10-20 km depth). However, since the ultimate goal of the modelling was to provide ground motions in the near- and intermediate field, we assumed that the synthetic earthquake takes place at a shallower depth (hypocentre at 5 or 7.5km).

In the following sections, we provide more detailed descriptions of the two modelling steps.

2.1 Generation of source models

2.1.1 Numerical method

The earthquake source models were generated by means of dynamic rupture modelling. This was performed using the 3DEC software package (Itasca, 2013), which is a 3-dimensional modelling tool based on the distinct element method (Cundall, 1971). 3DEC simulates the response of discontinuous media subjected to static or dynamic loading using an explicit time-stepping solution scheme. Joint planes can be kept active to model an assemblage of blocks or glued together to simulate a continuum. Blocks may behave either as rigid or deformable material. Deformable blocks are discretised using finite-difference elements and forces and relative movements along their boundaries are controlled by so-called subcontacts. 3DEC's capability to propagate waves properly has been verified by e.g. Fälth et al. (2015).

2.1.2 Model geometry

The model comprises a planar fault embedded in a finely discretized continuum. The dimensions of the model were set large enough to prevent the boundaries from influencing the solution within the simulation time, which was set long enough that the slip has time to be completed over the entire fault plane (Figure 4). We simulated both strike-slip and reverse faulting rupture scenarios. For the strike-slip scenarios the 5×5 km^2 fault plane is vertical (Figure 4a) while it has a dip angle of 29.52° with respect to the horizontal in the reverse slip scenarios (Figure 4b). The dip angle was set such that the fault is optimally oriented for failure according to Mohr-Coulomb theory, using a coefficient of friction of 0.6 (see Section 2.1.4). The upper edge of the fault plane is at 5 km depth in the strike-slip case and at 6.27 km depth in the reverse case.

Along the fault plane and within a distance of 0.5 km from the plane, the model discretisation length is 20.8 m, which allows for transmission of 20 Hz waves. Outside this volume the discretisation was made gradually coarser, and the discretisation lengths along the model boundaries are about 250 m. The model contains about 25 million finite-difference elements.

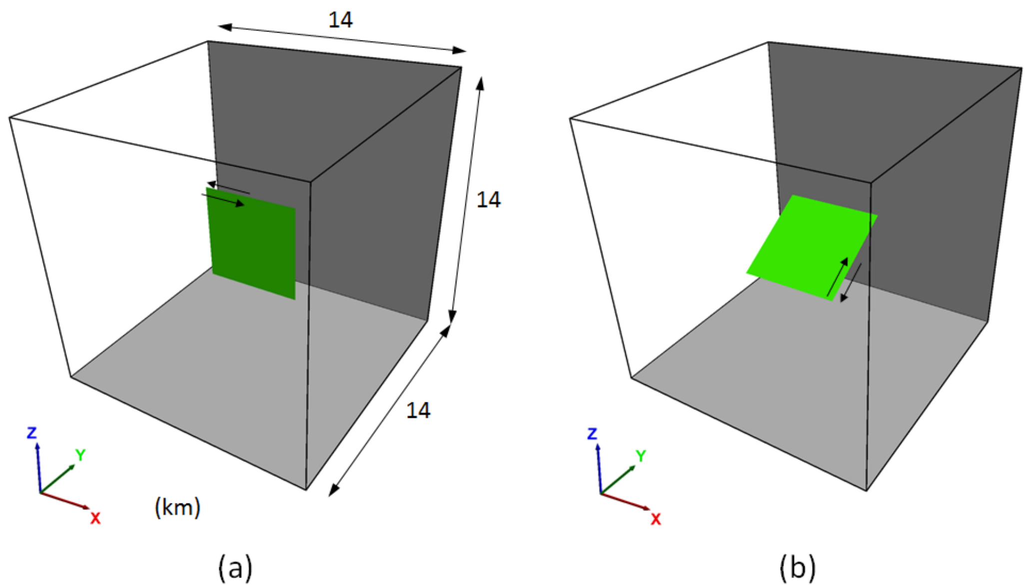

Figure 4. Model outlines and dimensions. (a) Strike-slip geometry and (b) reverse slip geometry. The outer dimensions are the same in both cases.

2.1.3 Governing laws and material properties

The rock mass surrounding the fault plane was modelled as a linear elastic, homogeneous and isotropic continuum. In the ground motion calculation in Compsyn, we adopted a layered velocity model of the crust that is typical for Nordic conditions (Table 4). Here in the 3DEC model, however, we only simulated an earthquake rupture occurring on a fault that spans a limited depth range. Thus, we adopted uniform mechanical properties, which are in agreement with the layered velocity model at the depth where the fault plane is located (Table 1). These property values yield seismic velocities of V_p = 6.1 km /s and V_s = 3.5 km/s.

To model the strength breakdown on the fault, we adopted the commonly used linear slip-weakening model (Ida, 1972), which means that the strength breakdown takes place over a certain amount of slip d_c. The fault frictional strength μ is modelled as a linear function of slip u, i.e.

$$\mu = \begin{cases} \mu_f + (\mu_u - \mu_f)\left(1 - \dfrac{u}{d_c}\right) & u \le d_c, \\ \mu_f & u > d_c \end{cases} \tag{1}$$

where μ_u and μ_f are the ultimate (static) and the final (dynamic) friction coefficients, respectively. The slip-weakening concept is illustrated in Figure 5. The parameter values used in the slip-weakening law were set such that the rupture velocity V_r stays below the shear wave velocity V_s of the surrounding medium and that a seismic moment corresponding to approximately M_w=5.5 was obtained (Table 1). However, when non-homogeneous fault properties were applied, the rupture velocity exceeded V_s locally at low strength locations.

To initiate the rupture, we adopted an approach described by Bizzarri (2010). Starting at the hypocentre (x^H, y^H, z^H), we enforced a radially expanding rupture to propagate at a constant rupture speed V_{force} = 0.5V_s within a nucleation region Σ_{nucl}. The friction coefficient was determined by

$$\mu = \begin{cases} \mu_{nucl} = \min\left\{\mu^{SW}, \mu^{tw}\right\} & ,\forall(x, y, z) \in \Sigma_{nucl} \\ \mu^{SW} & ,\forall(x, y, z) \notin \Sigma_{nucl} \end{cases} \tag{2}$$

where μ^{SW} is determined by Eq. (1) and μ^{tw} is given by

$$\mu^{tw} = \begin{cases} \mu_u - (\mu_u - \mu_f)\dfrac{(t - t_{force})}{t_0} & ,t - t_{force} < t_0 \\ \mu_f & ,t - t_{force} \ge t_0 \end{cases} \tag{3}$$

Here, Eq (3) is a time-weakening law, where the strength is ramped down linearly from μ_u to μ_f over a specified time t_0, and t_{force} is the time of rupture initiation at each location. At some time during the initiation process, the SW law (Eq. (1)) takes over and the rupture propagates spontaneously.

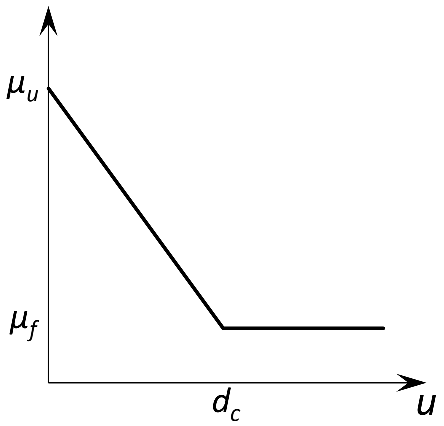

Figure 5. Linear slip-weakening law

We tested both the case of homogeneous fault frictional properties and the case of non-homogeneous properties. When we generate a non-homogeneous fault strength distribution, we acknowledge that natural fault surfaces are self-similar fractals, in the sense that their root-mean-square height fluctuations are proportional to profile length (Fang and Dunham, 2013 and references therein). Self-similar faults have a power spectral density

$$P \sim k^{-3}, \tag{4}$$

where k is wavenumber. Here, we did not model the surface roughness explicitly. Instead, to simulate the effect of surface undulations we applied a spatial variation of fault frictional strength with a self-similar distribution according to Equation (4). To obtain the desired spectral density, we generated 2D random Gaussian noise with zero mean, applied it to the fault plane and filtered it in the strike-slip and dip-slip directions. The resulting fault strength distribution $p(i,j)$ for the particular realisation we used here, normalised to its peak value, is shown in Figure 6. The mean value of the distribution is 0.0054, i.e. practically zero, as it should be. The normalised values $p(i,j)$ were multiplied with a scale factor h and added to the ultimate and final frictional coefficients at each fault location, i.e.:

$$\begin{aligned} \mu_u(i,j) &= \mu_u + h \cdot p(i,j) \\ \mu_f(i,j) &= \mu_f + h \cdot p(i,j) \end{aligned} \tag{5}$$

This means that we obtained spatial variations in fault strength that have mean values μ_u and μ_f. In the strike-slip case we set h = 0.04, i.e. such that the peak value of μ_f equals 0.6, which is the value we used when constructing the initial stress field (see Section 2.1.4). In the reverse slip case we set h = 0.0192, such that the minimum value of μ_u was kept above 0.6. Else, the fault would slip “in advance” at the weakest location.

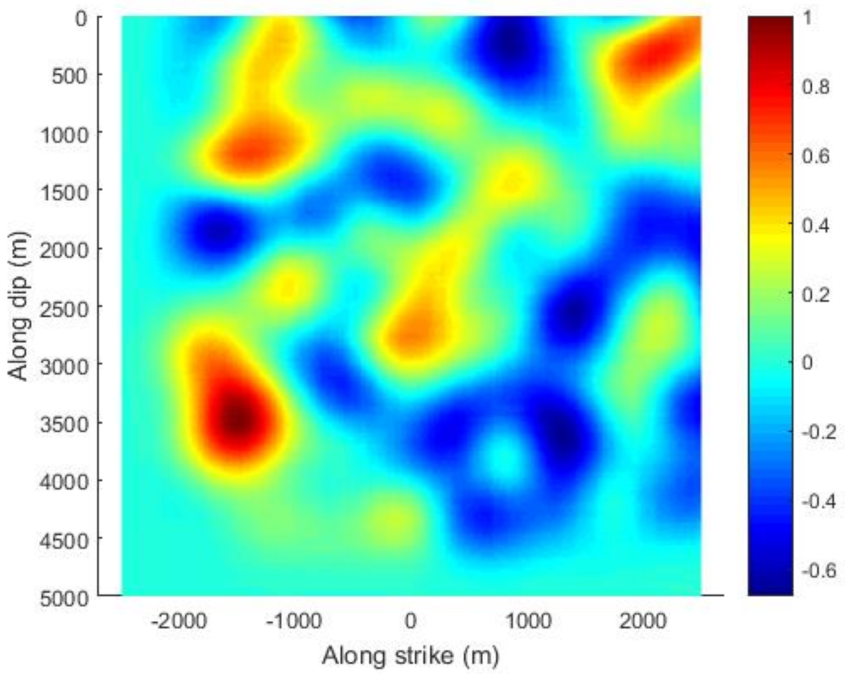

Figure 6. Normalised fault strength distribution for case #3.

Table 1. Material properties.

	Strike-slip	Reverse slip
Continuum:		
Young's modulus E (GPa)	84	
Poisson's ratio v	0.25	
Density ρ (kg/m^3)	2730	
Fault plane:		
Ultimate friction coefficient μ_u	0.65	0.618
Final friction coefficient μ_f	0.56	0.58
Scale factor for distributed fault strength h	0.040	0.0192
Slip-weakening distance d_c (m)	0.05	

2.1.4 Stresses

Data on stress magnitudes and stress orientations at depth are scarce. However, for this analysis where we created hypothetical rupture scenarios, it was not critical to have knowledge about the details of the stress field. What we needed was a stress field that yields a low stability on a major part of our fault plane such that spontaneous rupture propagation is possible. There are evidence indicating that the intraplate, continental upper crust is, in general and at some depth, in a state of frictional failure equilibrium on optimally oriented faults, see e.g. summary in Zoback and Townend (2001).We utilized stress fields that were constructed based on the assumption that the crust is in frictional equilibrium. For this we used the Mohr-Coulomb failure criterion, assuming frictional equilibrium on pre-existing, optimally oriented zones of weakness (e.g. Jaeger and Cook, 1979):

$$\frac{\sigma_1 - P}{\sigma_3 - P} = \left(\sqrt{\mu^2 + 1} + \mu\right)^2 \tag{6}$$

Here, σ_1 and σ_3 are the major and minor principal stresses, respectively, while P is pore pressure and μ is the coefficient of friction. To constrain the intermediate principal stress σ_2 we used (after Gephart and Forsyth, 1984)

$$R = \frac{\sigma_1 - \sigma_2}{\sigma_1 - \sigma_3} \tag{7}$$

We assumed that the vertical stress σ_v is a principal stress and that it is a function of depth, i.e. $\sigma_v = \rho g d$, where ρ is the density of the crust, g is the gravitational acceleration and d is depth. Using Equations (6) and (7), the stress magnitudes in a strike-slip stress field (for use in strike-slip rupture scenarios) could be calculated according to

$$
\begin{aligned}
\sigma_1 &= A(\sigma_3 - P) + P \\
\sigma_2 &= \sigma_v \\
\sigma_3 &= \frac{\sigma_2 - P(1-A)(1-R)}{A(1-R)+R} \\
\text{with } A &= \left(\sqrt{\mu^2+1}+\mu\right)^2
\end{aligned}
\tag{8}
$$

Similarly, we calculated the stresses in a reverse stress field (for reverse rupture scenarios) according to:

$$
\begin{aligned}
\sigma_1 &= A(\sigma_3 - P) + P \\
\sigma_2 &= \sigma_1(1-R) + \sigma_3 R \\
\sigma_3 &= \sigma_v
\end{aligned}
\tag{9}
$$

We assumed hydrostatic pore pressure, R = 0.5 and μ = 0.6. The normal to the two conjugate, optimally oriented fault planes, the two planes most likely to fail, have angles $\theta = \pm(90°–\text{atan}(\mu))/2$ with respect to the σ_3 orientation and are located in the σ_1–σ_3 plane. Thus, with μ = 0.6 we have θ = 29.5°. We oriented the stress field relative to the fault plane with 29.5° angle between σ_3 and the plane normal, and such that pure left lateral strike-slip events (Figure 4a) and pure dip-slip reverse events (Figure 4b) were generated.

2.1.5 Rupture scenarios

We modelled three left-lateral strike-slip faulting scenarios (Figure 4a) and two reverse faulting scenarios (Figure 4b), all with moment magnitude M_w ~ 5.5 (Table 2). We also recall here that the fault was square-shaped with edge length 5 km in all scenarios. In four of the scenarios the hypocentre was located at the centre of the fault plane at 7.5 km depth. However, in scenario #4, to examine the possible effects of the rupture propagating mainly downwards, we located the hypocentre at 5.5 km depth, closer to the fault's upper edge.

Table 2. Earthquake cases modelled in this study

Case	Hypocentre depth (km)	Fault type	Dip angle (deg)	Upper edge depth (km)	Notes
#1	7.5	Left-lateral strike slip	90	5	Homogeneous fault properties
#2	7.5	Reverse	29.5	6.27	Homogeneous fault
#3	7.5	Left-lateral strike slip	90	5	Non-homogeneous fault properties
#4	5.5	Left-lateral strike slip	90	5	Homogeneous fault properties
#5	7.5	Reverse	29.5	6.27	Non-homogeneous fault properties

2.1.6 Results

In Table 3, we present the earthquake source parameters. Even though we made changes in the hypocentre location and the fault strength distribution, the amount of average slip and the seismic moments are very similar for the scenarios. The values of average stress drop are also similar and on par with estimates of average stress drops for earthquakes worldwide, but are somewhat lower than estimates for intraplate events (e.g. Kanamori and Anderson, 1975).

The distributions of fault slip and rupture velocity are shown in Figure 7. There is a general tendency that the slip becomes larger at larger depths. This is because the stress drop scales with the stress level. Since the stress level increases with increasing depth, the stress drop also increases. A higher stress drop means larger associated slip.

We also note that the rupture speed tends to be higher in the mode II shear direction, which means along strike for a strike-slip case and along dip for a dip slip case (compare Case #1 and #2). This is in accordance with observations made in other studies (see e.g. Bizzarri, 2012). Furthermore, we note that among the cases with homogeneous fault properties, Case #4 generated the highest rupture speed. This is due to the hypocentre location close to the fault's upper edge, which means that there was a longer distance over which the rupture could accelerate. In addition, we see that the rupture speed exceeded V_s at low-strength locations in Case #3 and Case #5.

Table 3. Source parameters.

	Case #1	Case #2	Case #3	Case #4	Case #5
Seismic moment ($\cdot 10^{17}$ Nm)	2.22	2.20	2.22	2.20	2.19
Moment magnitude	5.49	5.49	5.49	5.49	5.49
Average slip (m)	0.27	0.27	0.27	0.27	0.26
Average stress drop (MPa)	4.20	4.16	4.23	4.36	4.20

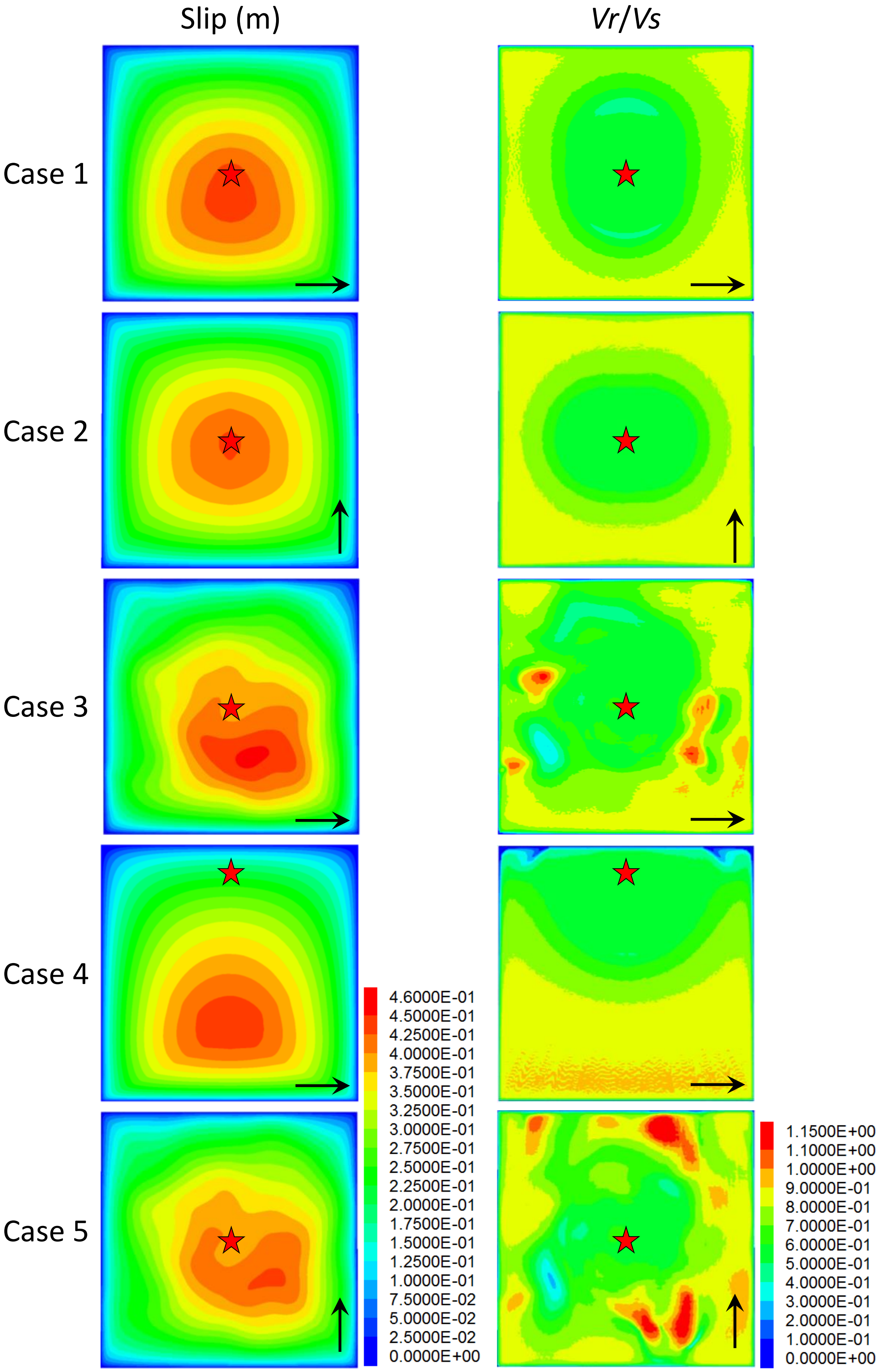

Figure 7. Contour plots of fault slip (left side) and rupture velocity-to-shear wave velocity ratio (right-side). The stars indicate the hypocentre locations and the arrows indicate the directions of slip.

2.1.7 Determination of Compsyn input

To create a rupture model suitable for Compsyn, we recorded the fault slip at a grid of recording points on the 3DEC fault plane and fitted linear time-slip functions in the strike-slip and dip-slip directions to the recordings. From these, we obtained slip function parameters for the corresponding grid of sub-faults in Compsyn.

To capture the details of the rupture process, it is desirable to have a dense recording grid, particularly when a spatial variation of fault properties is applied. However, as the grid density is increased the amount of output data increases quickly. Hence, one has to find a balance between the desire to refine the model and what is practically possible. Here, we used a 60×60 recording grid (3600 points) with a grid spacing of 83.3 m. We judge this recording grid to be dense enough given the spatial variation of fault strength we apply in Case #3 and #5, and given all other uncertainties involved in this problem. In Figure 8 we plot the normalised spatial strength variation along a horizontal scan-line at fault mid-height in Case #3. The x-positions of the crosses indicate the positions of the finite-difference element grid points in the 3DEC model while the squares indicate the positions of the recording points. The plot indicates that the potential effects of the strength variation should be captured in sufficient detail by the recording grid.

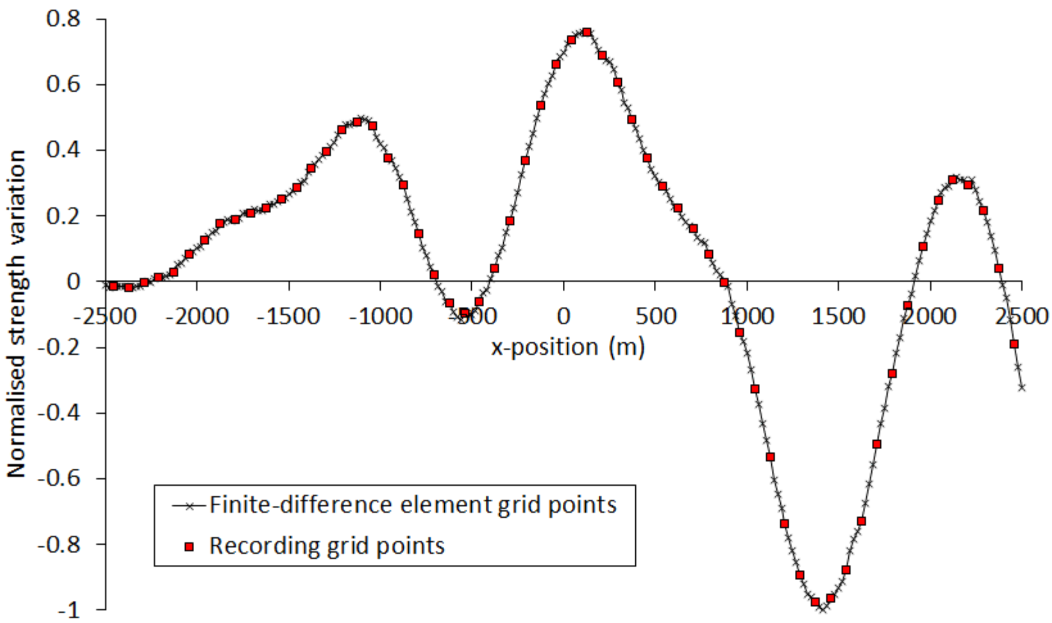

Figure 8. Frictional strength variation along a scan-line at the mid-height of the fault plane in Case #3. The cross markers indicate the x-positions of the finite-difference element grid points while the squares indicate the positions of the recording points.

When determining the slip function parameters for Compsyn, there are some restrictions. First, the same type of slip function is used on all sub-faults, and second, at each sub-fault, both time for onset of slip and rise time (time over which slip takes place) have to be equal in the dip-slip and strike-slip directions. However, time for onset of slip, rise time and slip velocity may be set individually for each sub-fault. We defined the slip initiation time as the time when the 3DEC slip velocity exceeds 0.05 m/s. Given the slip initiation time and final total slip value, the rise time in the linear Compsyn slip function was set such that the integrals of the 3DEC time-slip function and the linear Compsyn time-slip function were equal. The fitting was performed using a MATLAB script, which also generates the file with input parameters used by Compsyn. Examples of the fit of the linear slip functions to the 3DEC output data are shown in Figure 9.

The agreement of the slip initiation times and the resulting slip is illustrated by the contour plots in Figure 10.

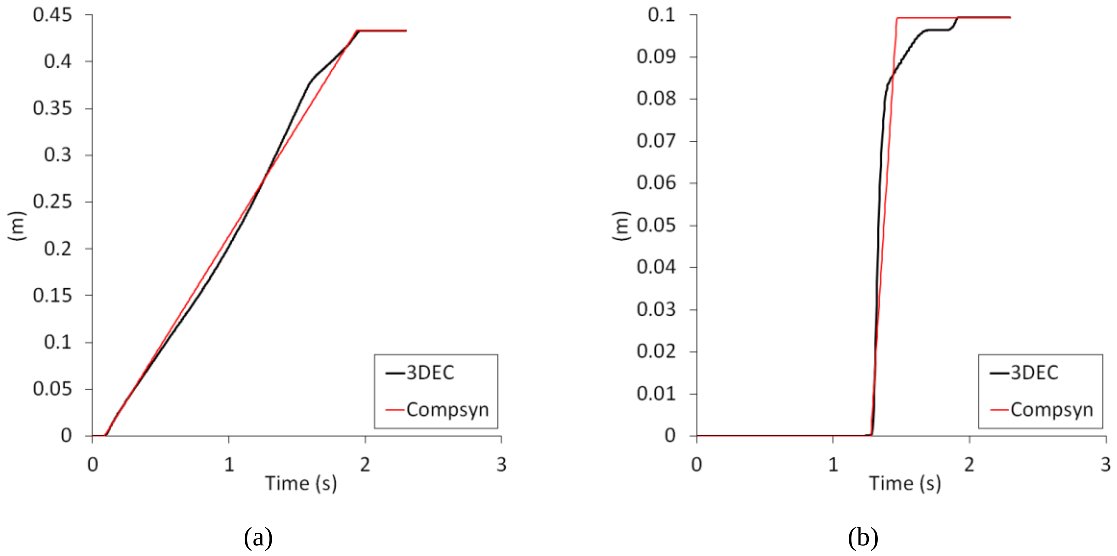

Figure 9. Examples of fit of linear time-slip functions to the 3DEC slip data in Case #1 at (a) a point close to fault centre and (b) at a point close to fault's upper edge.

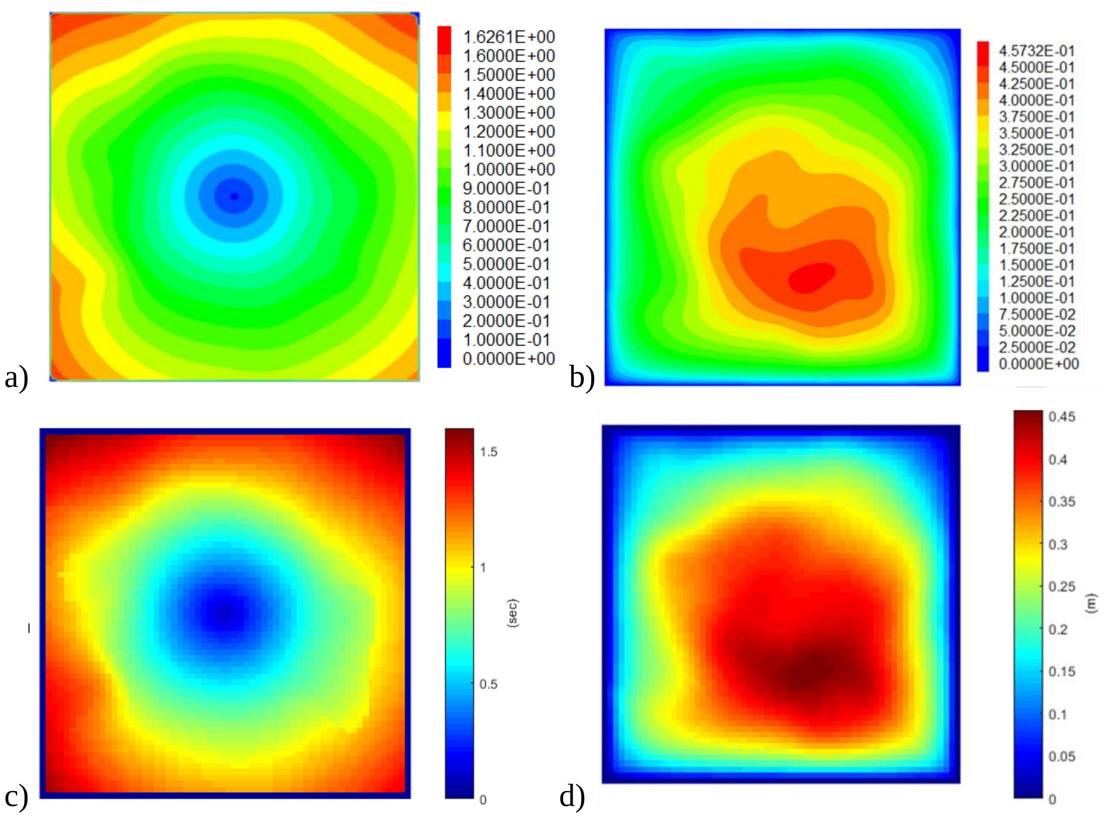

Figure 10. Case #3. Slip initiation times (sec) from 3DEC model (a) and as transferred to Compsyn (c); Fault slips (m) as generated by the 3DEC model (b) and the fitted slip model applied in Compsyn (d). Note the "pixels" in the Compsyn model. Each "pixel" corresponds to one of the 3600 sub-fault.

2.2 Wave propagation modelling

When ground motions are simulated it is a reasonable assumption to model the crust as an elastic medium. It carries pressure (P-) and shear (S-) waves from the source to the ground surface. The Earth's crust was modelled as a vertically layered medium in order to account for the significant changes in density and velocities as a function of depth.

The velocity profile of the medium was typical for Fennoscandian conditions (Table 4). Shallower depths are characterized by the slowest seismic velocities. Each layer boundary in the earth model is a discontinuity creating reflection, transmission and refraction of waves. Waves may also diffract around obstacles, an effect ignored it this simulation. The depth of the model is limited to 42 km, since the aim of the modeling is to predict vibrations at the distance of maximum 28 km from the epicenter.

Table 4. Velocity model used in the Compsyn models

Depth (km)	Pressure P-wave (m/s)	Shear S-wave (m/s)	Density (g/cm^3)
0.0	5300	3100	2.65
0.8	5800	3300	2.72
15.0	6450	3750	3.02
42.0	6890	3900	3.07

The most important discontinuity in the model is the ground surface. The free surface produces Rayleigh waves, and together with other discontinuities in the Earth, Love waves. The Rayleigh wave contains P- and the SV component of S-wave whereas the Love wave contains the SH component of the S-wave. The SH- and SV denote shear waves in horizontal and vertical directions relative to the ground surface, respectively. All mentioned waves propagate with different velocities and on measured ground motions one is able to pinpoint the different wave arrivals. However, at close vicinity of the epicenter the waves arrive within a short time interval and may overlap with each other, while at longer distances wave arrivals separate significantly. In the software package used here the discrete wavenumber element method was used to compute synthetic waveforms (Olson et al., 1984). In the method, the P- SH- and SV-waves are described with first order differential equations in a cylindrical coordinate system and solved with the finite element method (Olson et al., 1984), (Kennedy et al., 1981), (Bolt, 1987).

The simplest earthquake source is a point source which is good approximation for small earthquakes and medium sized earthquakes at larger distances. A more sophisticated approach for larger events is point source summation using kinematic slip functions and complete Green's functions. Point source summation is a method in which a fault is represented by a grid of nodes, each node acting as a source inducing displacement and stresses in the elastic media.

The synthetic ground motions for this work were computed with the Compsyn package (Spudich and Xu, 2003). Compsyn incorporates the point source summation and complete Green's functions for slightly modified discrete wavenumber element method to compute synthetic waveforms. With point source summation it is possible to compute slip with third party software such as 3DEC and use the result as input to Compsyn. The strength of Compsyn is that it computes the complete response of the considered earth structure including all P-, S- and surface waves. However, the computation effort for higher frequency content is significant, due to the required number of elements in the discrete wavenumber method to represent high frequency content. Compsyn does not restrict highest possible frequency of a simulated waveform, but in practice large-area simulation of the ground motion could be done up to 15.0 Hz, and even higher frequencies can be simulated at restricted location of interest. Alternatively, Compsyn should be coupled with another simulation package for high frequencies such as ISOSYN (Spudich and Xu, 2003).

Another limitation is that the attenuation due to inelasticity outside of the fault area cannot be taken into account with Compsyn. However, the geometrical attenuation is included.

As discussed earlier, the scenario was a moment magnitude $M_w = 5.5$ earthquake, modelled with slip on a rupture area of 5×5 km^2. The slip values on the rupture area were obtained from 3DEC in 60×60 recording points and linearized, according to the procedure described earlier. The rupture-time, rise-time and slip velocity resulting from this linearization were transferred to Compsyn.

The first concern was to show that the 3DEC and Compsyn model were compatible, and that the transfer of fault movements was done correctly. For this purpose we used the Case #1 model to benchmark the output of the two codes. Ground surface displacements were calculated at a few locations (stations) from both 3DEC and Compsyn. Because of the computational limitations of 3DEC, the benchmarking stations were chosen close to the fault (Figure 11).

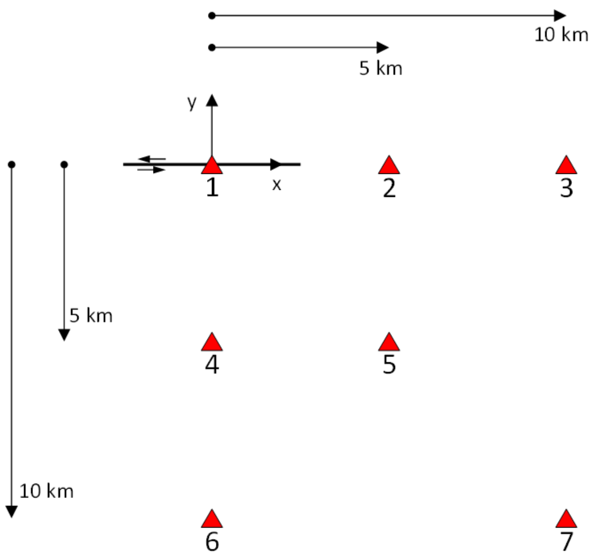

Figure 11. Locations of ground surface benchmarking stations for comparison of output from the 3DEC and Compsyn models

The 3DEC model was discretized with 20.8 m elements, for output up to 20 Hz in the immediate vicinity of the rupture. However, the mesh was gradually coarsened such that the element edge length was about 250 m at the model boundaries. With the boundaries of the 3DEC model quite close to the stations, it can be expected that waves reflected from the boundaries will affect the 3DEC model. Hence, the comparison had to be done in the initial few seconds of the wave propagation and for frequency content up to 2-3 Hz.

Correspondingly, Compsyn output was produced for content up to 10 and 25 Hz. In this case the computational limitations were less severe compared to those of 3DEC.

The comparison of displacements at stations 2 and 7 (Figure 11) are presented in Figure 12 and Figure 13. As expected, station 2 which is on the nodal plane only experiences y-direction movement. Some numerical noise can be noticed in all 3DEC model plots. Taking into account the scale different between the vertical axis of the graphs, it can be seen that in Figure 12 only Figure 12.b correspond to real displacements. Figure 12.a and Figure 12.c show numerical noise for the 3DEC model and zero displacement for the Compsyn model. Otherwise the results are compatible. The 3DEC model y-displacement starts to deviate from the constant static displacement at around 8 s. This is attributed to the arrival of boundary reflection waves.

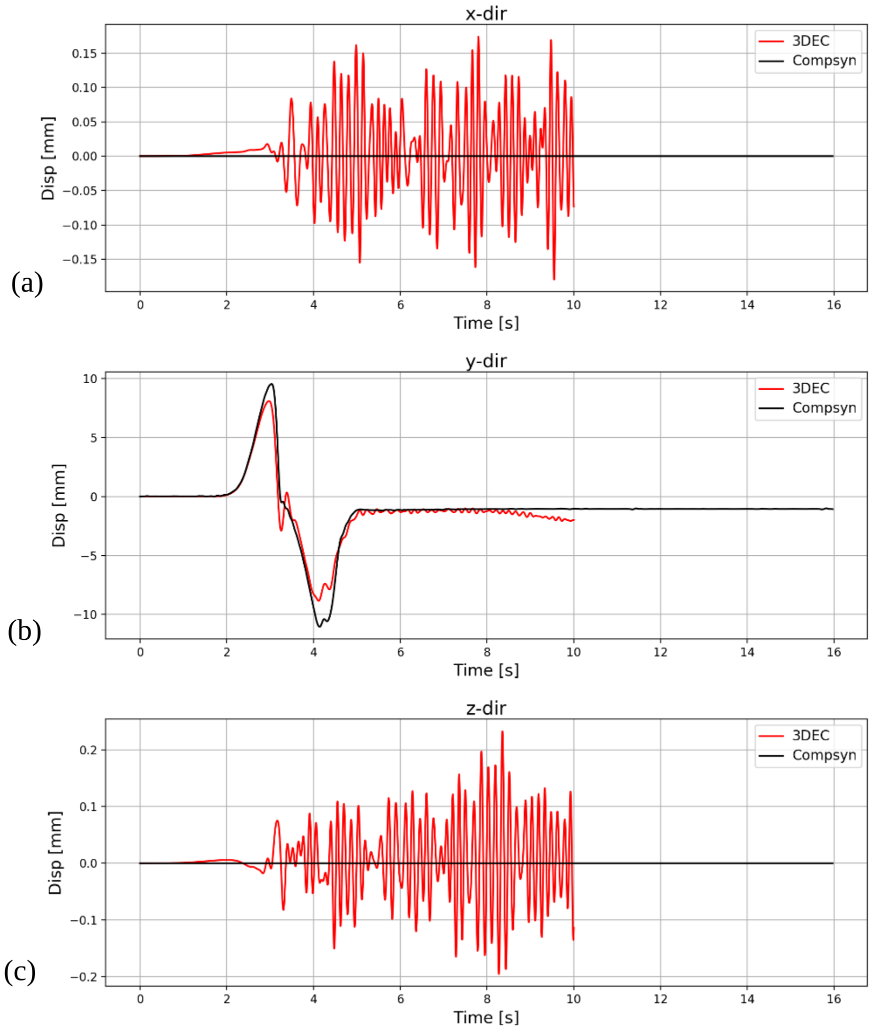

Figure 12. Ground surface displacements at station 2, in model Case #1 from 3DEC and Compsyn

Similar comparison is presented from station 7 in the Figure 13. It can be noted that the two models are in good agreement in the initial phase, up to about 6 s. The deviation of the 3DEC curve starts in this case at about 6-7 s, and partly overlaps with the direct wave. This is consistent with the idea of interference from reflected wave, as station 7 is closer to the model boundaries than station 2. The comparative plots for all benchmarking stations from Figure 11 show that the differences between the 3DEC and Compsyn models are in the ranges presented for these two output stations.

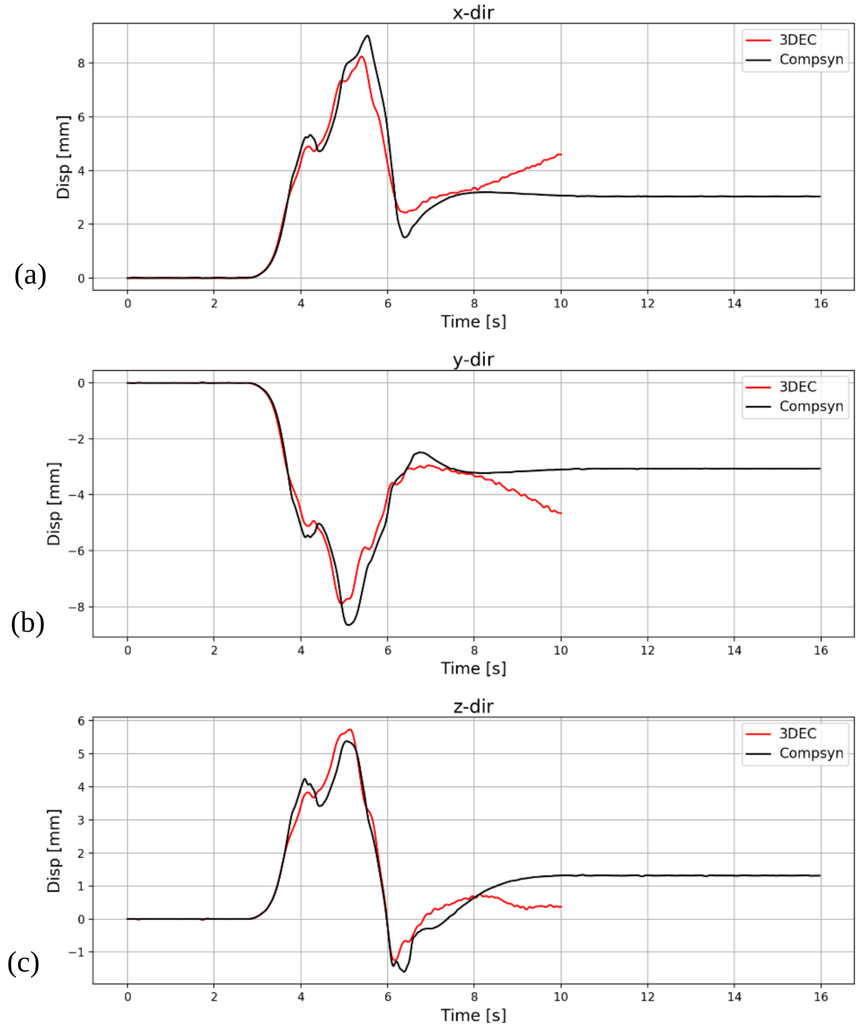

Figure 13. Ground surface displacements at station 7 in model Case #1 from 3DEC and Compsyn

We conclude that the 3DEC and Compsyn models produce effectively identical output for the Case #1 model at the two stations shown here as example. At the other five stations (Figure 11) we obtain similar fits. Since the same transfer protocol was used for the fault slip in the Case #2, #3, #4 and #5 models, we are confident that the fault movements in Compsyn are similar to those of 3DEC also for these models.

3 Simulated ground motions

In the next phase, we produced larger area outputs with the Compsyn models. We used a target output frequency of 10Hz, and generated output in a grid of 1×1 km at the ground surface. Such dense output permitted the animation of the motion propagation and static displacement on the ground surface, in order to facilitate visual inspection of the results.

The displacements in the longitudinal, transvers and vertical directions were plotted at several time-steps in Figure 14, Figure 15, Figure 16, Figure 17 and Figure 18 for each considered case. In Figure 14, Figure 16 and Figure 17, the expected ground motion pattern generated by the vertical fault moving in a pure strike-slip direction can be observed. However, the ground motion pattern is more complex in Figure 15 and Figure 18, which depicts ground motion of the gently dipping fault. As expected, the displacement patterns are symmetric around the y-axis in the cases with homogeneous fault properties (Case #1, #2 and #4). The impact of the fault inhomogeneity is manifested as a slight disturbance of the symmetry during the dynamic evolution of the displacements (compare the 5.9 s plots in Figure 14 and Figure 16 as well as the 5.9 s plots in Figure 15 and Figure 18). The arrival time of the wave train varies slightly.

The scenarios with a gently dipping fault (Case #2, #5) and the scenario with a shallower hypocenter (Case #4) have about 0.3 s earlier arrival times than Cases #1 and #3 (Table 2). At time instance 4.1 s and 5.9 s Figure 14, Figure 15, Figure 16, Figure 17 and Figure 18 shows the wave propagation. At 8.0 s in radial and transversal directions, there were still some propagating waves visible on circular pattern with radius ~15km. The colorful lobes inside these circles indicate static ground displacement. It can be noted that the reverse slip earthquake gives significantly large static displacements than the strike-slip cases.

All considered scenarios have locations of strong polarization in which one of the horizontal components are close to zero whereas the other one is some large number in terms of displacement. These regions correspond to locations close to the extension of the fault planes in the strike-slip case (Figure 14, Figure 16 Figure 17) where radial displacement is zero. The same applies for locations close to positions perpendicular to the fault-plane. Transversal displacements are close to zero at locations aligned at about 45° with the fault plane direction.

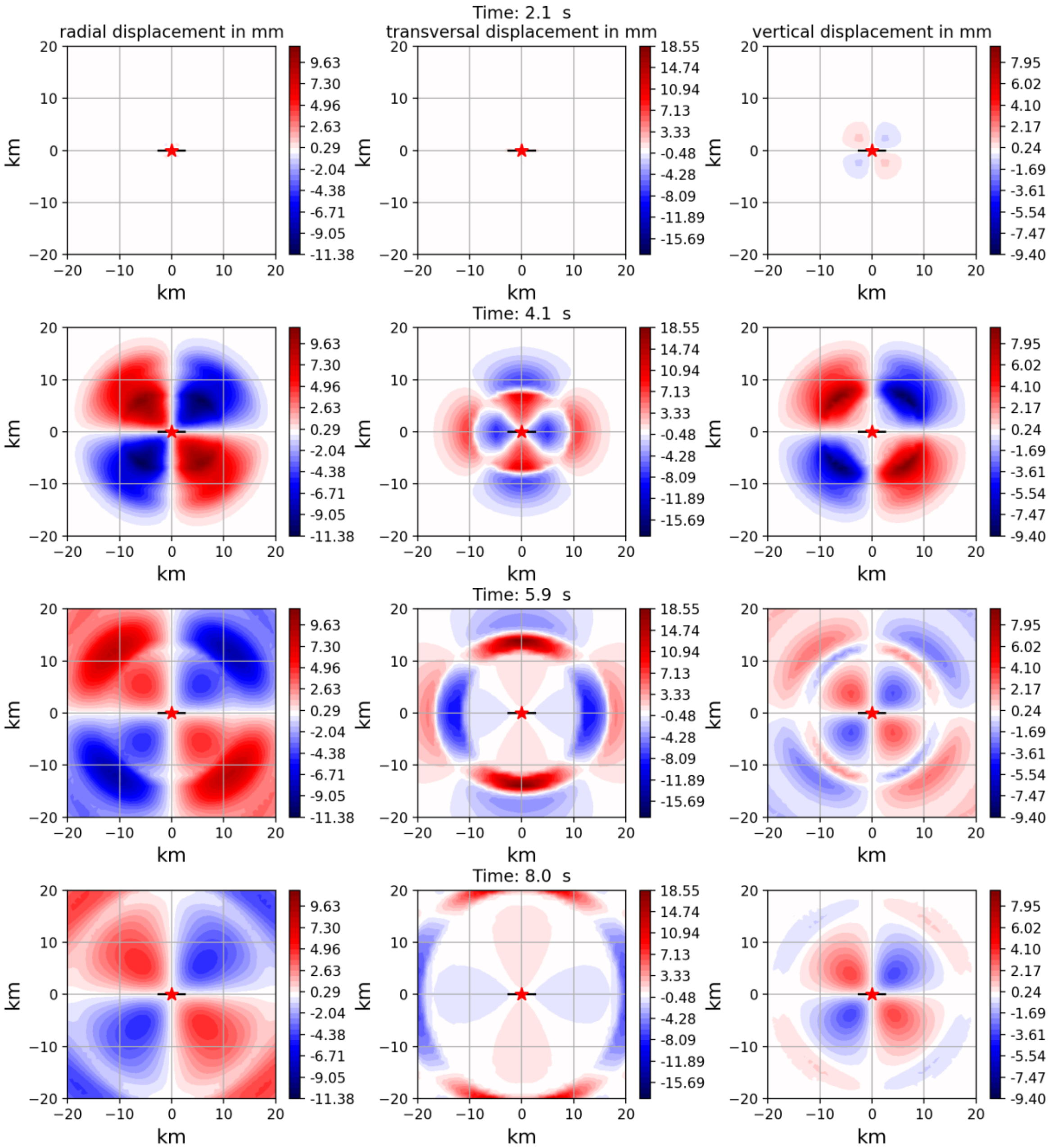

Figure 14. Propagation of the waves, at the ground surface, from the rupture of a 5×5 km^2 fault (Case #1). The vertical fault is visible as a thick black line, and the epicentre as a red star. At 2.1 s after rupture initiation the pressure waves emerge. The 4.1 s and 5.9 s plots show wave propagation, and finally, at 8.0 s propagating waves are further than 15 km. Blue and red lobes within 15 km radius from the epicentre are static ground displacements in millimeters.

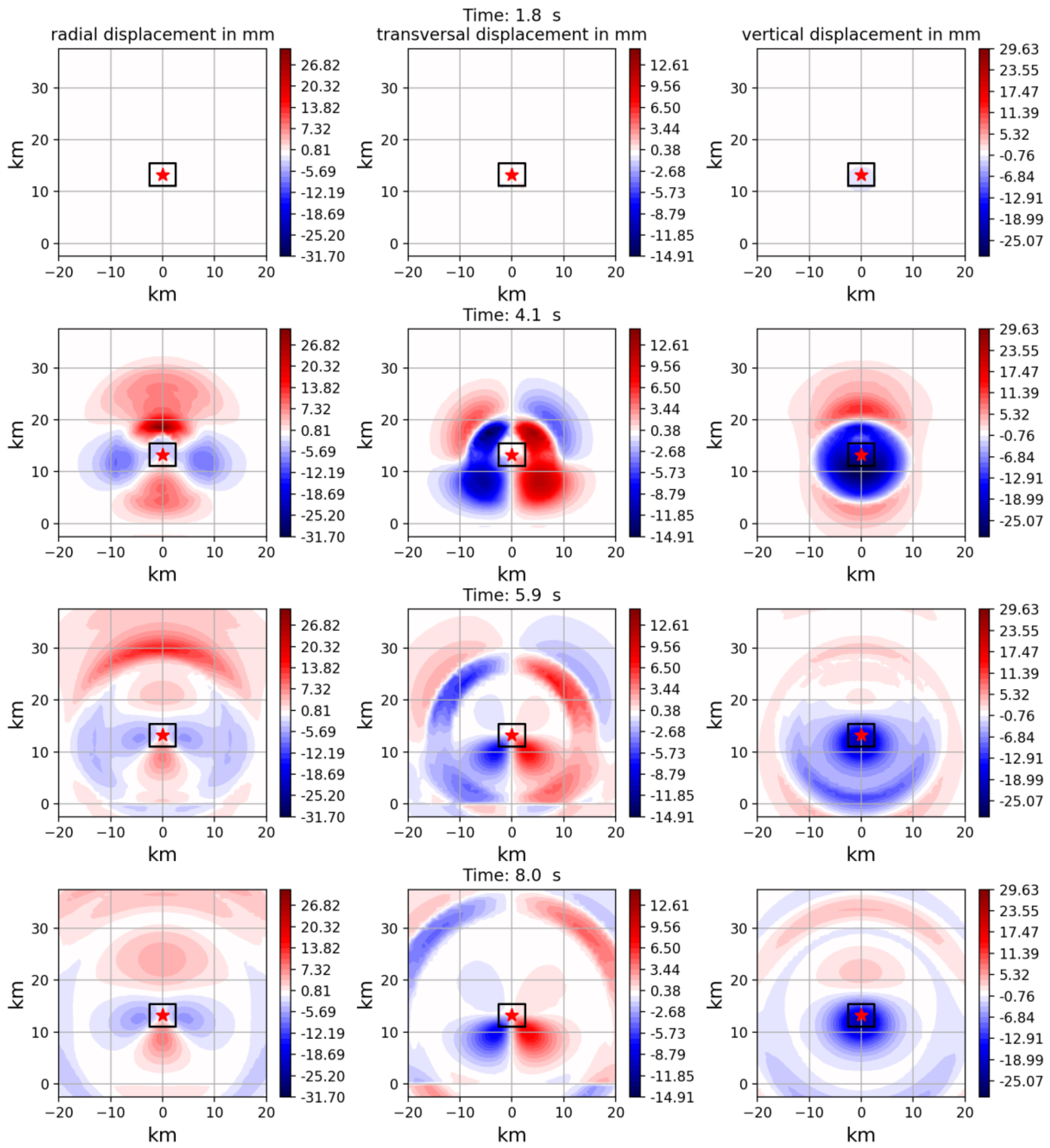

Figure 15. Propagation of the waves, at the ground surface, from the rupture of a 5×5 km^2 fault (Case #2). The dipping fault is visible as a thick black rectangle, and the epicentre as a red star. At 1.8 s after rupture initiation, the pressure waves emerge. The 4.1 s and 5.9 s plots show wave propagation, and finally, at 8.0 s propagating waves are further than 15 km. Blue and red lobes within 15 km radius from the epicentre are static ground displacements in millimeters.

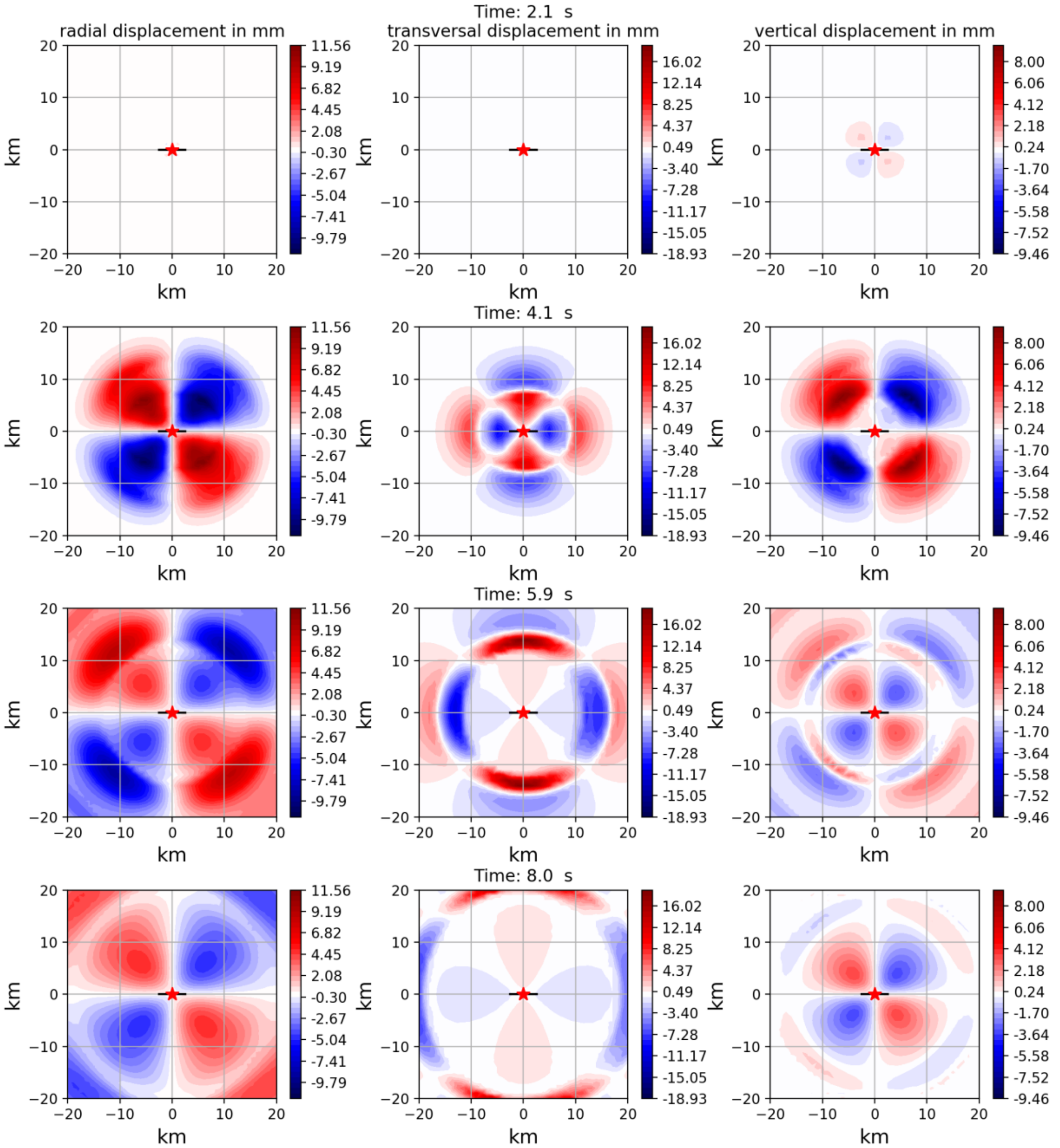

Figure 16. Propagation of the waves, at the ground surface, from the rupture of a 5×5 km^2 fault (Case #3). The vertical fault is visible as a thick black line, and the epicentre as a red star. At 2.1 s after rupture initiation, the pressure waves emerge. The 4.1 s and 5.9 s plots show wave propagation, and finally, at 8.0 s propagating waves are further than 15 km. Blue and red lobes within 15 km radius from the epicentre are static ground displacements in millimeters.

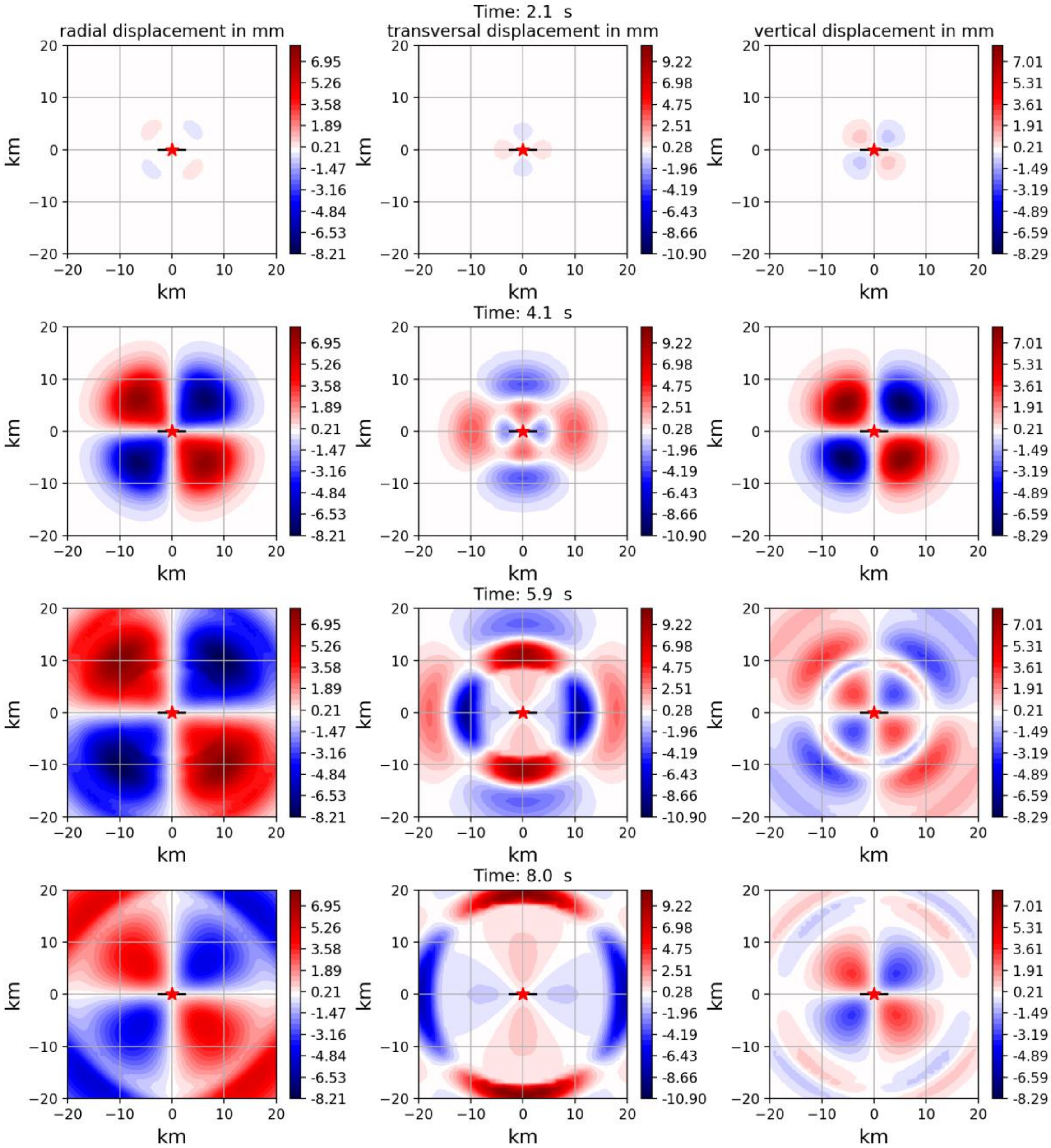

Figure 17. Propagation of the waves, at the ground surface, from the rupture of a 5×5 km^2 fault (Case #4). The vertical fault is visible as a thick black line, and the epicentre as a red star. At 1.8 s after rupture initiation, the pressure waves emerge. The 4.1 s and 5.9 s plots show wave propagation, and finally, at 8.0 s propagating waves are further than 15km. Blue and red lobes within 15 km radius from the epicentre are static ground displacements in millimeters.

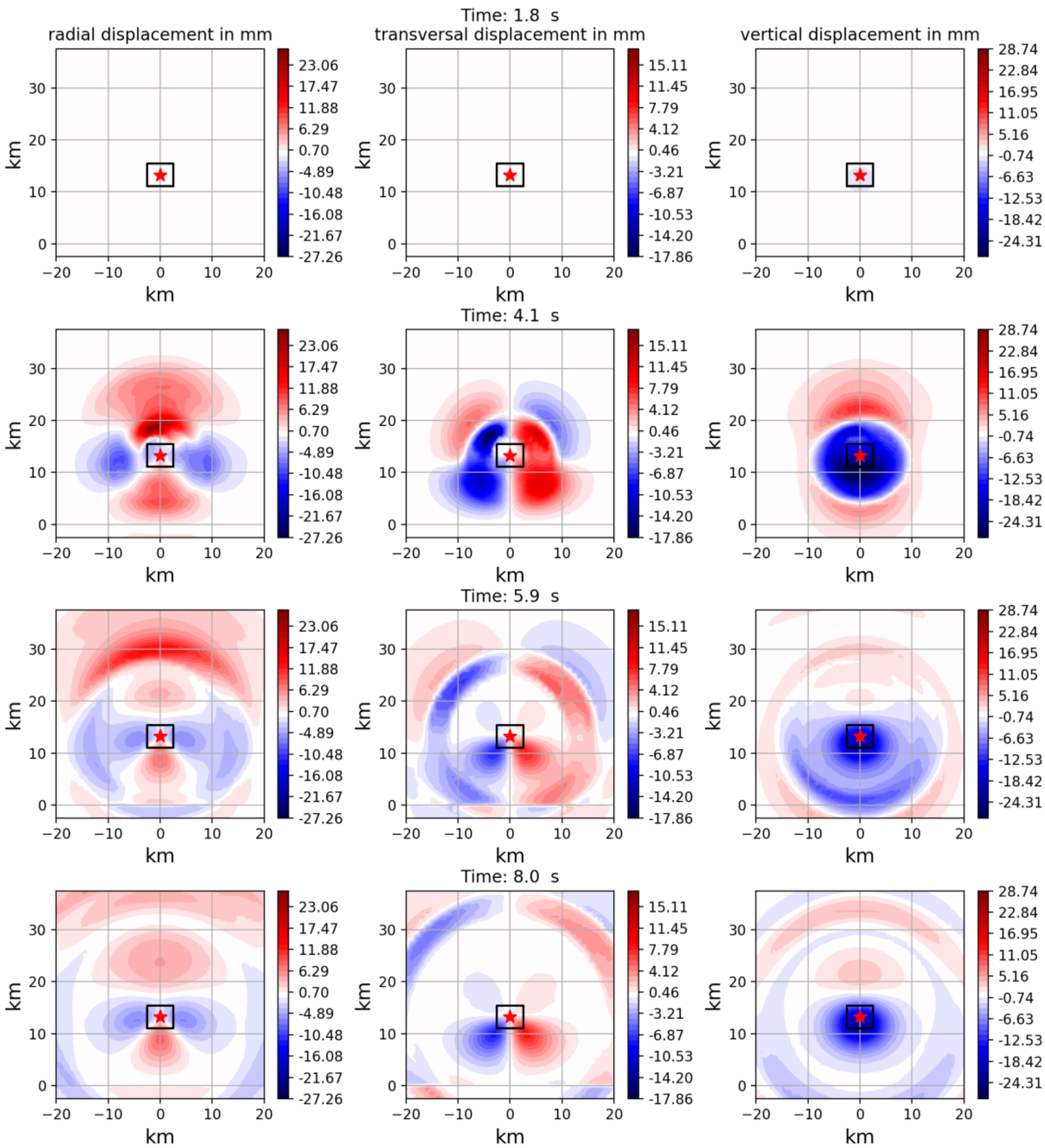

Figure 18. Propagation of the waves, at the ground surface, from the rupture of a 5×5 km^2 fault (Case #5). The dipping fault is visible as a thick black rectangle, and the epicentre as a red star. At 1.8 s after rupture initiation, the pressure waves emerge. The 4.1 s and 5.9 s plots show wave propagation, and finally, at 8.0 s propagating waves are further than 15 km. Blue and red lobes at 15 km radius from the epicentre are static ground displacements in millimeters.

4 Selection of empirical data for comparison

In the range of moment magnitude M_w=5.5 earthquakes there are no digital recordings available in Fennoscandia. For smaller magnitudes, we could use recordings or existing GMPEs from Fennoscandia to compare our synthetic model results to, or we could use international data and/or GMPEs for the comparison. However, because of the shear wave velocity V_{s30} exceeding 3000 m/s in Fennoscandia, the choices for earthquake recordings and GMPEs is limited.

The obvious candidate for comparisons were the recent GMPEs based on Fennoscandia data (Vuorinen, 2015). There are two formulations given by Vuorinen (2015) calibrated to the same dataset. We refer to them as the new Fennoscandian GMPEs (NF-GMPE) in the text.

The third GMPE, was the G16 model developed for central and eastern North America (Graizer, 2016). G16 was chosen as an alternative comparison model, in addition to the Fennoscandian models. We choose G16 instead of earlier formulations from the same region (e.g. Toro, 2002) because it is recent and incorporates the latest measurements in the stable continental part of North-America.

Hence, below we attempt a tree-way comparison between the synthetic model outputs, G16 developed for stable continental regions incorporating M5.5 events and the NF-GMPEs calibrated with smaller magnitude earthquakes (M≤5). While NF-GMPEs were calibrated for smaller magnitude data, Vuorinen, (2015) provides a comparison of the models with data up to M6 from stable continental regions in south-east Canada. These comparisons showed good fit of the NF-GMPEs with the data.

4.1 GMPE computation procedure

The GMPEs are developed for a certain range of frequencies of the acceleration spectra calculated from earthquake recordings. They express the level of ground shaking and its associated uncertainty as function of event distance and moment magnitude. The level of ground shaking is usually expressed in the peak ground acceleration (PGA) or spectral ordinate at a set of frequencies (SA_f).

Normally three acceleration recordings are available at each observation location. They are two horizontal perpendicular directions and one vertical direction. GMPEs can be calibrated to horizontal ground motion or vertical ground motion, but all GMPEs used here are for horizontal ground motion.

When GMPEs predict horizontal ground motion, a typical procedure has been to combine the two perpendicular horizontal ground motion components into a single measure in terms of PGA or SA_f.

A commonly used method to combine components has been by calculating geometric mean (GM) of the level of ground shaking. However, if ground motions are polarized and one direction component is very small, GM is a bad measure since it predicts close to zero combined ground shaking. A remedy for the situation is to use more sophisticated directional combination methods, e.g. RotD50 suggested by Boore et al., (2006) and Boore (2010).

Another disadvantage of the GM combination method is that combined intensity is not independent of the orientation of the two components. Basically, this means that the resulting combined PGA/SA_f depend on the orientation of the instruments measuring the two horizontal ground motion components, adding to the randomness of the data and increasing the uncertainty of the prediction. Combination methods like RotD50 remove this uncertainty, making the combined ground shaking intensity independent of the direction of measurement. Hence, they are often called direction independent.

The important differences between the GMPE used here are:

- NF-GMPEs are calculated in geometric mean (GM) while the G16 in RotD50;
- NF-GMPEs are expressed in acceleration (SA), while G16 in pseudo-acceleration (PSA). This is only a semantical difference, since SA is equal to PSA in all frequencies of interest and damping levels used in this study (see e.g. Mentrasti, 2008).

4.2 The G16 ground motion prediction equation

G16 was developed to express the horizontal peak ground acceleration (PGA) and 5% damped pseudo-spectral acceleration (PSA) RotD50 component. As mentioned earlier, RotD50 is a direction independent measure of the horizontal PSA (Boore et al., 2006). The GMPE has the following limitations (Graizer, 2016):

- 450 m/s<V_{s30}<2800 m/s
- 3.75<M_w<6 (proposed up to M=8.5 by author)
- 0<Dist<1000 km

G16 is based on formulations for PGA and PSA prediction based on "filters" set-up to account for different physical effects observed in seismic wave propagation. The distance used in G16 is the rupture distance.

$$PGA = G_1 \cdot G_2 \cdot G_3 \cdot G_4 \tag{10}$$

Where: G_1 is a filter for magnitude scaling;

G_2 is the core attenuation equation;

G_3 is a filter for anelastic attenuation;

G_4 is the site correction filter;

To what concerns the G_4 site correction factor, the calibration data was available for V_{s30}=450-2000 m/s, with V_{s30}=640 m/s the average shear wave velocity of the dataset. The correction factor G_4 was calibrated using equivalent linear software using time history analysis (Kottke and Rathje, 2009), with validation based on models extended up to V_{s30}=2800 m/s. Since the site conditions of Finnish NPP correspond to even higher shear wave velocity (V_{s30}>3000 m/s) the G16 model will be used up to its validity limit and studied for V_{s30}=3100 m/s in order to be fully compatible with the model outputs.

The spectral shape is formulated based on normalized spectra, with corrections for the site amplification:

$$PSA(T) = PGA \cdot PSA_{norm} \cdot Lin_{Amp} \tag{11}$$

Where: T is the period of the spectra calculated;

PSA_{norm} expressed the normalized spectral shape;

Lin_Amp controls the linear site amplification;

In Figure 19.a we show how the G16 model predicts PGA at various distances and for various magnitudes. The shape of the spectra predicted by G16 varies both with the earthquake magnitude and with distance. For the distance of R_{rup}=50km, the spectral shape predicted by G16 are given in Figure 19.b for different magnitudes.

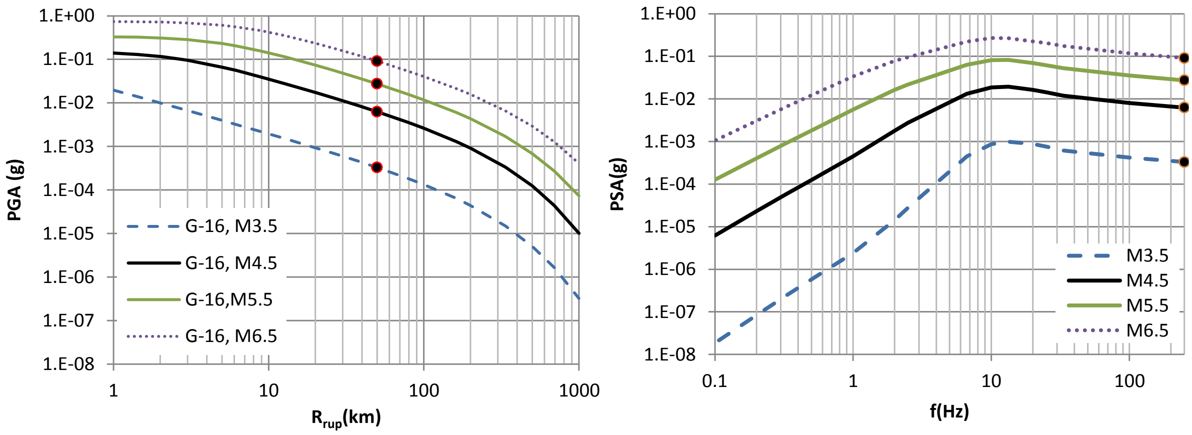

(a) (b)

Figure 19. (a) PGA with rupture distance predicted by G16 for M=3.5…6.5 earthquakes and soil with V_{S30}=2800 m/s and (b) PSA spectra variation with magnitude at rupture distance R_{rup}=50 km and soil with V_{S30}=2800 m/s

4.3 New Fennoscandia NF-GMPEs

Recently new Fennoscandian ground motion prediction equations were published (Vuorinen, 2015). Two models, an empirical model (EMP-GMPE) and a reference empirical model (REF-GMPE) were calibrated to Finnish and Swedish measurement data. These models are expressed in geometric mean of the spectral acceleration (SA).

The EMP-GMPE equation form is based on Pezeshk et al., (2011), while constants are fitted based on the data. It is defined as follows:

$$\begin{gathered} log_{10}(\bar{Y}(f)) = c_1 + c_2 M_w + c_3 M_w^2 + (c_4 + c_5 M_w) \\ \times min\{log_{10}(R), log_{10}(70)\} + (c_6 + c_7 M_w) \\ \times max[min\{log_{10}(R/70), log_{10}(140/70)\}, 0] \\ +(c_8 + c_9 M_w) \times max\{log_{10}(R/140), 0\} \\ +c_{10} R \end{gathered} \tag{12}$$

where,

$$R = \sqrt{R_{Rup}^2 + c_{11}^2} \tag{13}$$

where $\bar{Y}(f)$ is the median value of the PGA or SA in g, f is a considered frequency in Hz, M_w is the moment magnitude, c are constants calibrated using nonlinear least-squares regression from the available seismic measurements and R_{Rup} is the closest distance to fault rupture in km.

The REF-GMPE relies as well on the curve given by Pezeshk et al., 2011. In order to fit the PGA/SA to the Fennoscandia conditions, the REF-GMPE is scaled as follows:

$$log_{10}(\bar{Y}_{ref}(f)) = log_{10}(F) + log_{10}(\bar{Y}(f)) \tag{14}$$

where

$$log_{10}(F) = c_0 + min(M_w - M_{min}, 0) \times \left[c_1 + c_2 \times min\left(R_{Hyp} - 70\right), 0\right] \quad (15)$$

where

$M_{min} = 5.0$ and the hypocentral distance R_{Hyp} was approximated as:

$$R_{Rup} \approx R_{Hyp} \cong \sqrt{R_{Ep}^2 + d^2} \quad (16)$$

where R_{Ep} is an epicentral distance and d is a measured depth of the event. In the scaling of the REF-GMPE the constants in the scaling function Eq. (15) were calibrated to the Fennoscandia data in order to fulfil local conditions.

The new Fennoscandian GMPEs have the following limitations:

- V_{s30} not documented, but mostly recorded on hard-rock >3000 m/s
- $0.5<M_w<4/4\text{-}8$ (for EMP-GMPE and REF-GMPE depending on frequency)
- 1<Dist<1000 km

The "c" constants were calibrated for ten frequencies between 0.5 Hz and 100 Hz.

EMP-GMPE was used to predict PGA for earthquake magnitudes M=3.5 and 4.5 with rupture distance (Figure 20.a). These magnitudes and distances are within the calibration range of the GMPE. The PGA prediction of the EMP-GMPE was also compared to G16, in the range of magnitudes 3.5-6.5 (Figure 20.b). It can be noticed that, in the range of magnitudes 3.5-4.5 the fit between the two is good.

4.4 Analysis the GMPEs with regard to PGA

In order to show the limitations of using ground motion prediction equations outside of their calibration range, we report a comparison of the G16 with EMP-GMPE for magnitudes M=3.5, 4.5, 5.5 and 6.5 (Figure 20.b).

The plots of the two types of GMPEs in Figure 20.b are not fully compatible. For instance, it is supposed that the 100 Hz spectral value has no amplification in the EMP-GMPE, but there is already some amplification compared to the PGA in G16. It also has to be emphasised that G16 is using RotD50 as measure, while the EMP formulation is using geometric mean (GM).

The two predictions fit reasonably well for M=3.5 and M=4.5, both magnitudes in the calibration range of the two GMPE formulas. However, already for M=5.5 and especially for M=6.5 the EMP formulation severely over-predicts the PGA. These two magnitudes are outside of the calibration range of the EMP-GMPE, and it was advised in the original publication that the EMP-GMPE is badly constrained outside of its calibration range (Vuorinen, 2015).

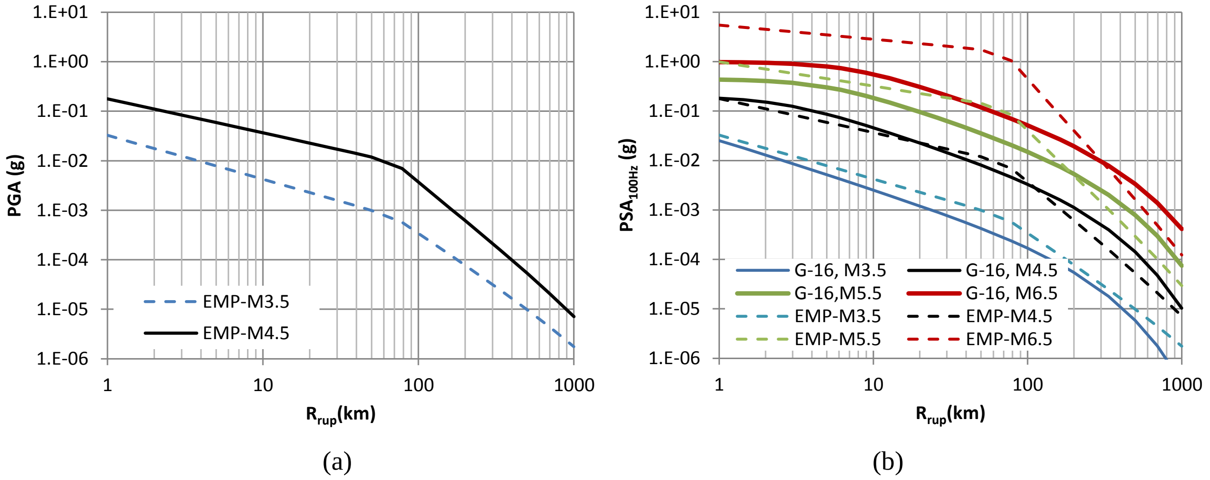

Figure 20. (a) PGA attenuation with rupture distance predicted by EMP-GMPE for M=3.5…4.5 earthquakes. Soil conditions are unknown, but data is from Fennoscandia and filtering was used to remove recordings suspected to be affected by soft-soil response. (b) Comparison of the G16 prediction for 100Hz and that of EMP-GMPE for 100Hz for a range of magnitudes. It should be noted that the M5.5 and M6.5 predictions are outside of the calibration range for EMP-GMPE

4.5 Analysis of the GMPEs with regard to spectral shape and criticism of the new Fennoscandia GMPE

EMP-GMPE was also used to predict the spectral shapes (Figure 21). The plots should be compared to the spectral prediction of G16 illustrated earlier in Figure 19.b. The curve corresponding to M6.5 was not plotted in Figure 21, because it is out of the calibration range of EMP-GMPE. The shape of the spectra predicted by EMP-GMPE is completely unexpected and evidently incorrect, because it does not show a tendency of decrease towards the low frequencies (left-side).

For oscillators with increasing flexibility, towards the left side of the plot, the response has to show a decreasing trend (see Figure 19.b for comparison). This is because more flexibility means less connection to the ground, hence less excitation transmitted to the oscillator mass. In the extreme case of complete flexibility the response of the oscillator to ground shaking would be zero. The plot in Figure 21 stops at a 0.5Hz oscillator, but at this frequency the downwards trend of the plot should be clear, especially for recordings on hard rock.

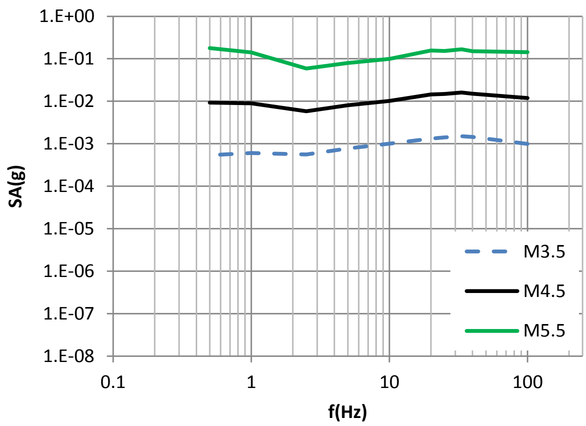

Figure 21. SA spectra variation with magnitude at constant rupture distance R_{rup}=50 km based on the EMP-GMPE formulation. Rock conditions (V_s~3000 m/s) as all data were from Fennoscandia.

The effect can probably be attributed to the way of combining the horizontal components to form the geometric mean spectra. As stated on Page 21 of Vuorinen (2015) the "*PGA and 5% damped response spectral acceleration at 9 selected frequencies, ranging from 0.5 Hz to 40 Hz, were computed from the geometric mean of horizontal registrations.*" Hence, the spectral computation procedure for the Fennoscandian GMPEs is as follows:

(1) Compute geometric mean of the horizontal components at desired location.

$$GM(t) = \sqrt{a_1(t) \cdot a_2(t)} \tag{17}$$

where $GM(t)$ is the geometric mean, $a_1(t)$ and $a_2(t)$ are horizontal acceleration components.

(2) Compute response spectra (SA) from the resulting geometric mean signal.

This approach has significant shortages. The Eq. (19) leads to the complex arithmetic if $a_1(t)$ or $a_2(t)$ is negative. In order to avoid complex arithmetic the absolute value of $a_1(t)$ and $a_2(t)$ was used in Eq. (19). As a result the geometric mean acceleration *GM(t)* is always larger than zero. This also implies steadily increasing displacement, even before arrival of p-wave. Therefore, the computation process is non-physical and in our opinion incorrect (Jussila et al., 2017).

Based on test calculations, we estimate that the methodology results in reduction of spectral peaks by a factor of about two (i.e. 100%) and a shift of the spectral peaks towards higher frequencies.

Hence, we suggest that new Fennoscandian GMPEs should not be used in hazard predictions, especially for predicting uniform hazard spectra (UHS), until they are updated and the *c* constants recalibrated. Since there are no significant deviation in PGA between the different methods of combining horizontal components(see Figure 5-3 in PEGASOS, 2004b), the error introduced here for PGA is probably limited to 15-25%.

As the new Fennoscandian GMPEs have been calibrated on data derived by non-standard procedure, the modelling results of this study will be compared to outputs of G16 only.

5 Comparison of modelling results to the G16 predictions

The comparisons are done in terms of spectra between results extracted at the recording stations in Figure 11 and the G16 prediction for the same rupture distance for modelling Cases #1, #2, #3, #4 and #5 (Figure 22 - Figure 26).

It has to be remembered that the Compsyn models were calibrated to produce output up to 25 Hz. Hence, the synthetic recordings have no signal above this frequency, while the G16 prediction is calibrated up to 250 Hz. It also has to be mentioned that G16 was used here with V_{S30}= 3100 m/s. This makes the two predictions equivalent in terms of V_{s30}, but G16 was calibrated only up to shear wave velocity of 2800 m/s (Graizer, 2016). Hence an extrapolation of G16 is used. However, the effect of setting slightly higher shear wave velocity produces very reasonable behaviour with G16, i.e. the PGA is slightly reduced.

As it can be noticed in Figure 22, the comparison of the model outputs for Case #1 with G16 is mixed. In most stations the comparison is reasonable, but e.g. the model gives very low values in station 1 compared to the G16 prediction. The same behaviour can be noticed for Case #3 and Case #4.

This is caused by the model scenario used here (Case #1, #3, #4), which implies that the fault is perfectly vertical and only strike-slip (i.e. horizontal) motion, takes place on the fault. The ground motion patterns for these cases were given in Figure 14, Figure 16 and Figure 17, showing clear regions of low vibration in-line with the fault, perpendicular to the fault and at 45 degs. As visible from the 4.1s plot of the vertical displacements (Figure 14), waves are emerging at a certain distance from the centre of the plot, resulting in a relatively quiet epicenter region.

The same quiet epicenter region does not exist for the reverse-slip faults in Case #2 and Case #5 (Figure 22, Figure 26).

Fault rupture in reality is complex, e.g. having both strike and dip direction components. Faults are also not vertical and perfectly plane. The focal mechanism gives a strong bias if a single event is used, and the velocity model may not be fully representative for the area where the data for G16 comes from. Hence, real ground motion patterns are much less systematic. With other shortcomings of this comparison, we can conclude that the results are reasonable, given the complexity of the modelling problem.

The results shown in Figure 22 - Figure 26 are based on results extracted at the seven ground surface stations shown in Figure 11. It can be noticed that the most severe under-prediction of the model in Case #1, #3, #4 occurs at the epicentre location, station 1 (x=y=0, d_{rup}=5 km), while other outputs are in the reasonable range.

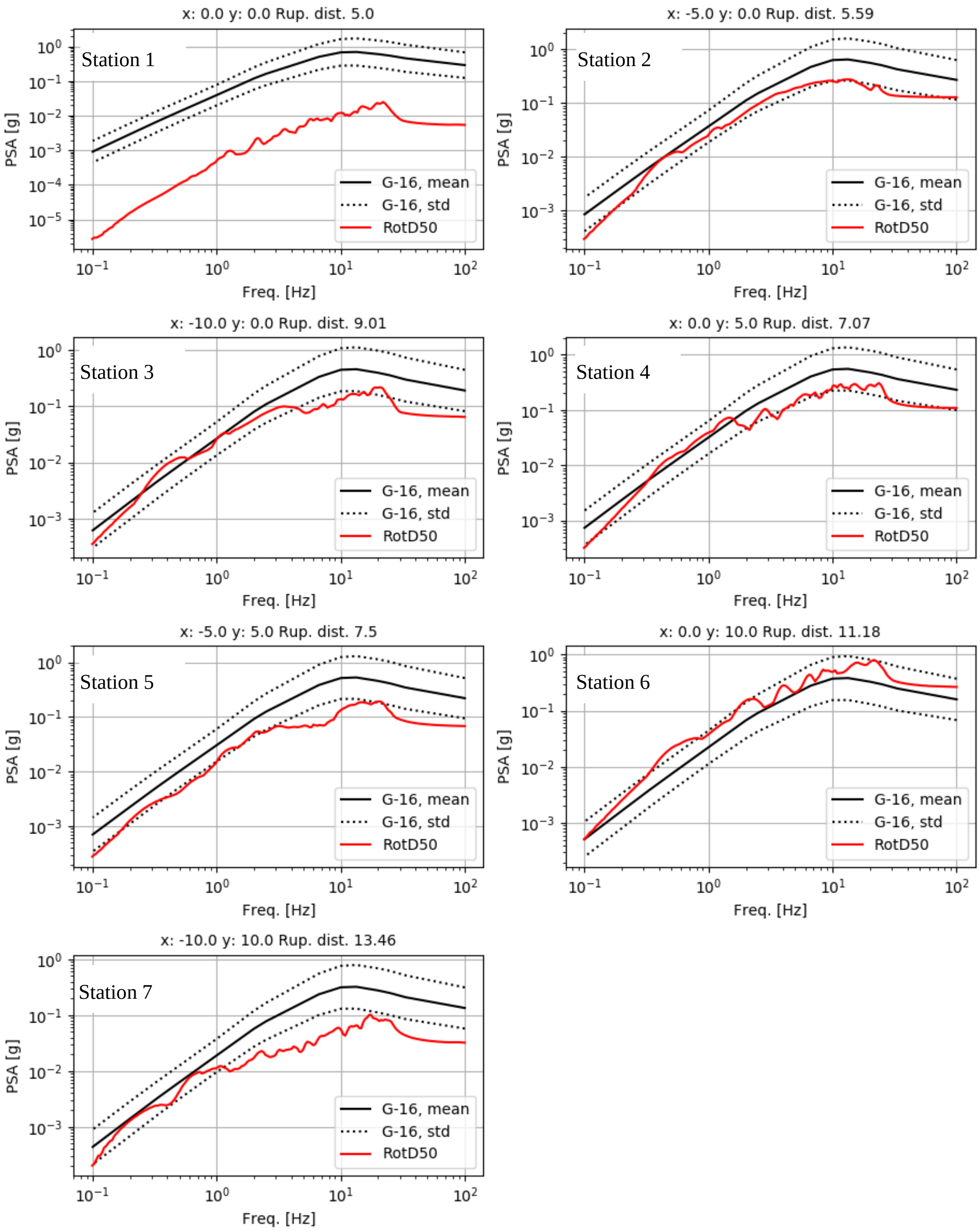

Figure 22. PSA spectra comparison between the G16 prediction and the Case #1 model outputs. Red lines are the model outputs (RotD50). Continuous black line is the mean prediction of G16, while dashed lines are the ± 1 standard deviation bounds predicted by G16. Station numbers refer to the ones given in Figure 11.

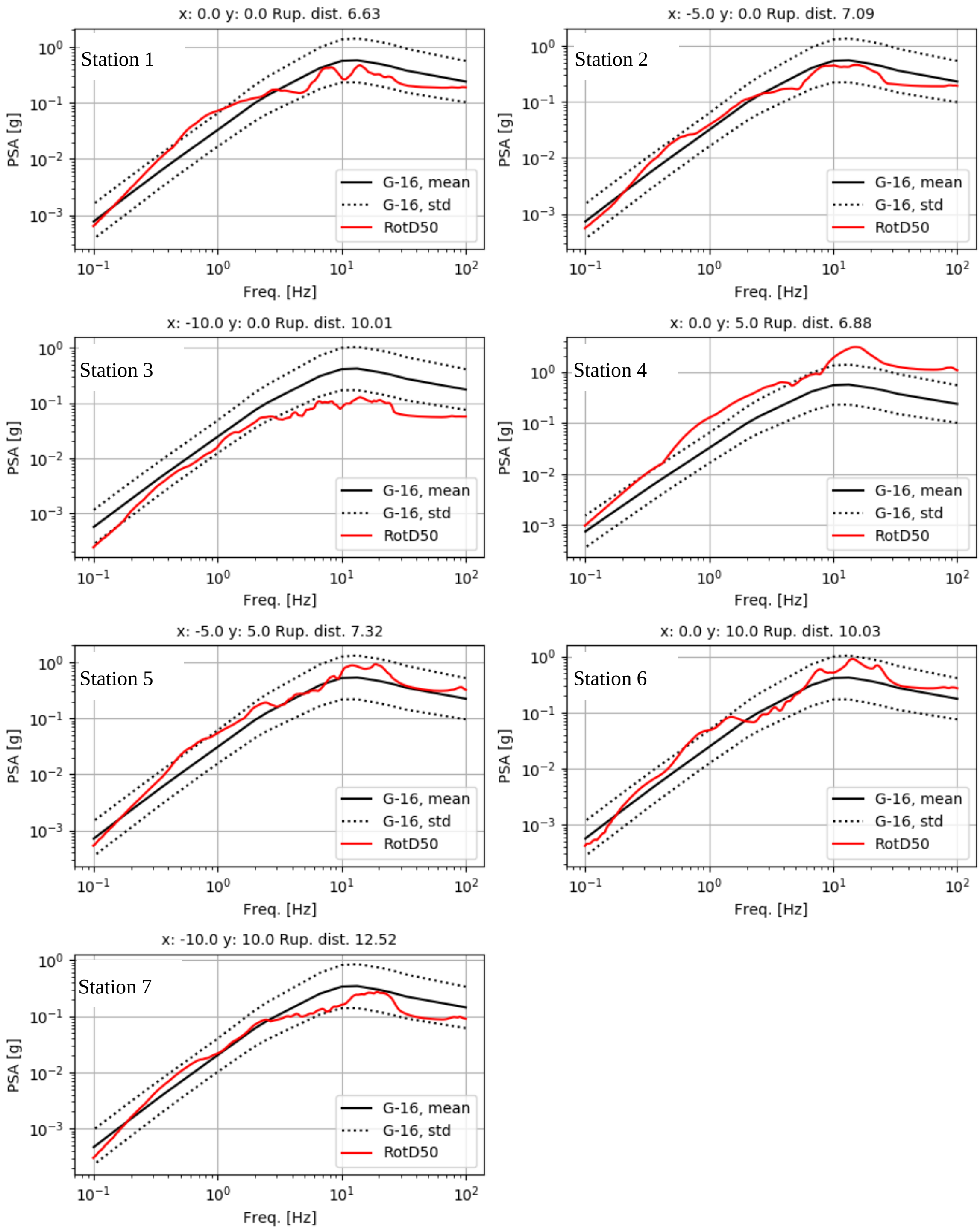

Figure 23. PSA spectra comparison between the G16 prediction and the Case #2 model outputs. Red lines are the model outputs (RotD50). Continuous black line is the mean prediction of G16, while dashed lines are the ± 1 standard deviation bounds predicted by G16. Station numbers refer to the ones given in Figure 11.

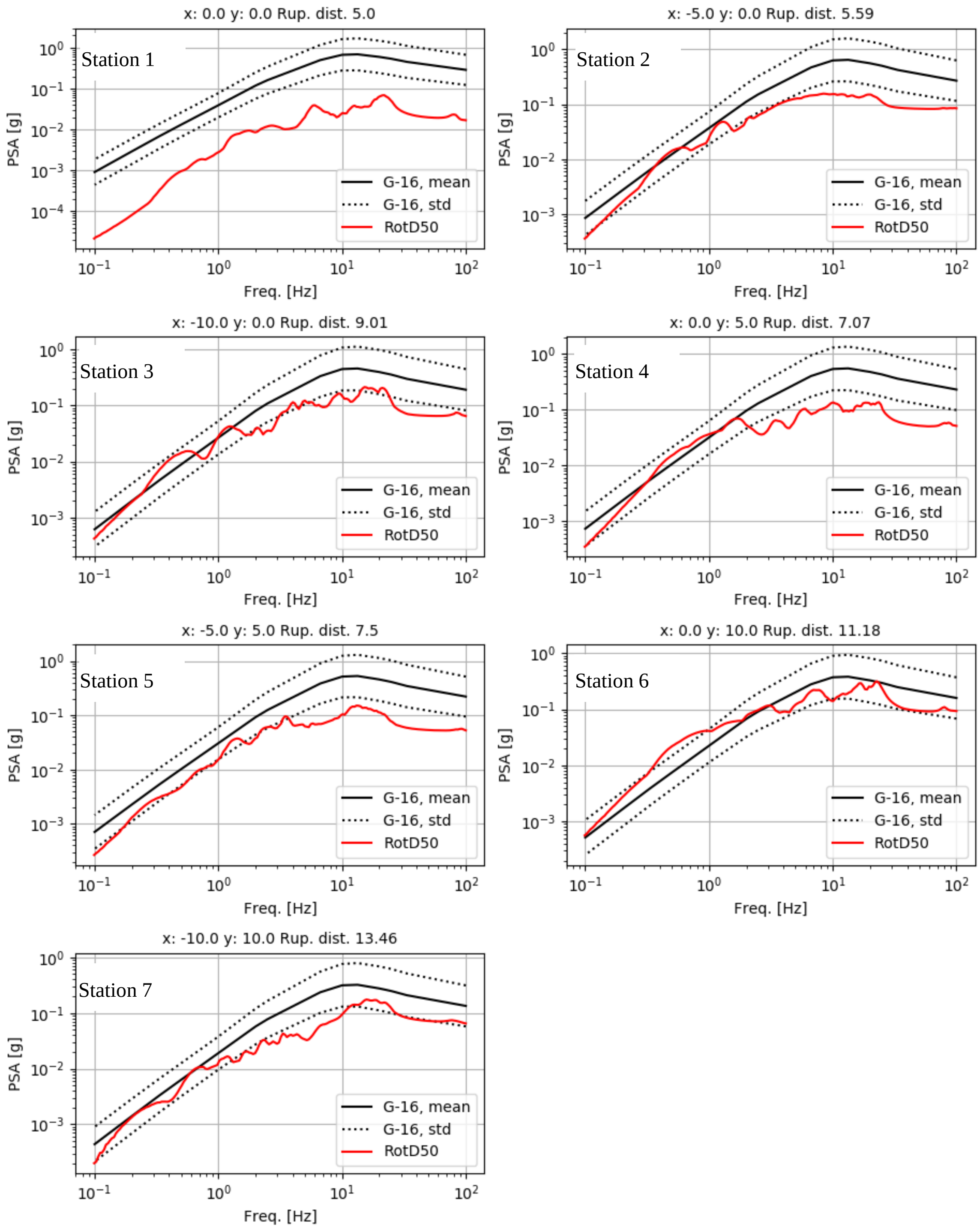

Figure 24. PSA spectra comparison between the G16 prediction and the Case #3 model outputs. Red lines are the model outputs (RotD50). Continuous black line is the mean prediction of G16, while dashed lines are the ± 1 standard deviation bounds predicted by G16. Station numbers refer to the ones given in Figure 11.

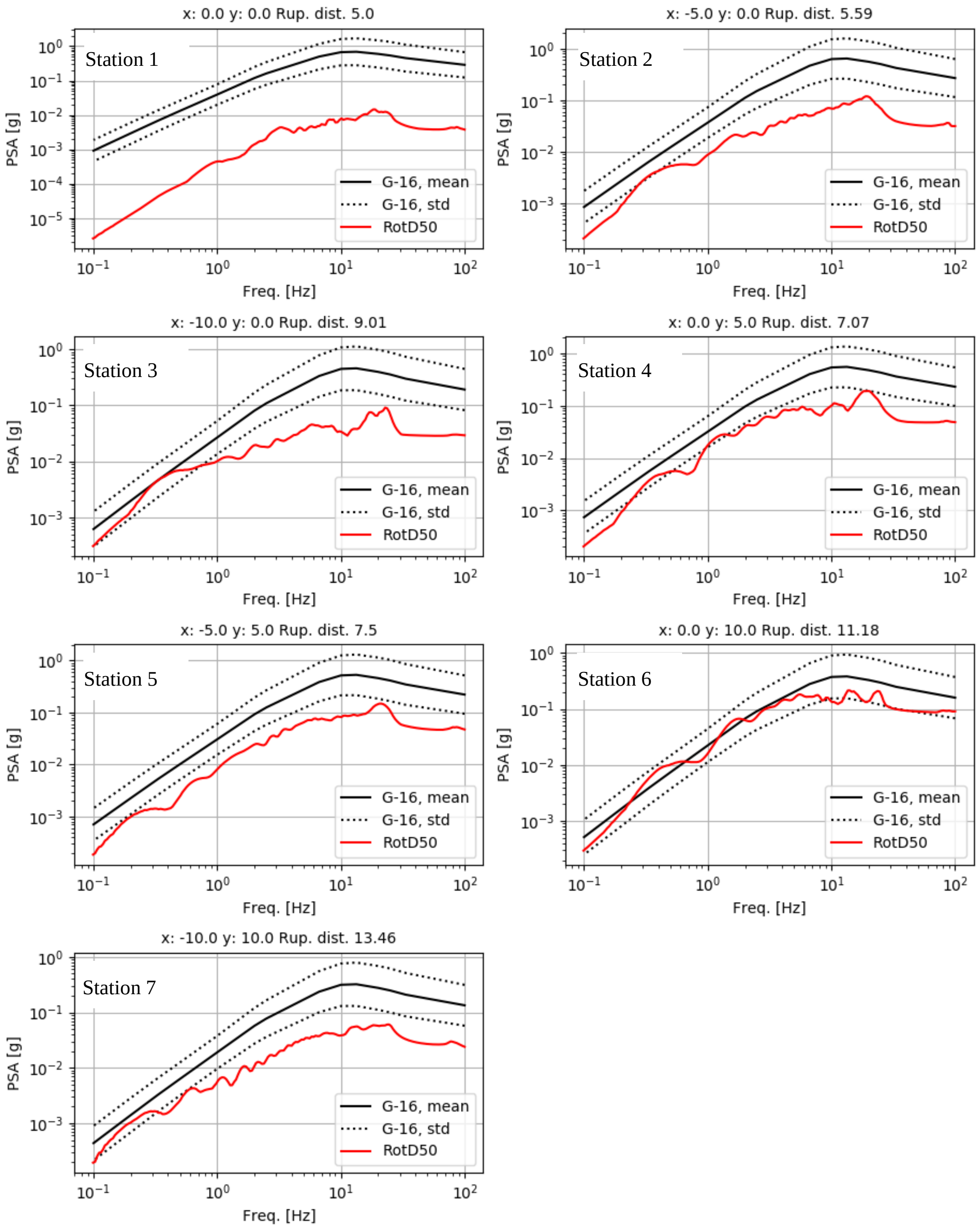

Figure 25. PSA spectra comparison between the G16 prediction and the Case #5 model outputs. Red lines are the model outputs (RotD50). Continuous black line is the mean prediction of G16, while dashed lines are the ± 1 standard deviation bounds predicted by G16. Station numbers refer to the ones given in Figure 11.

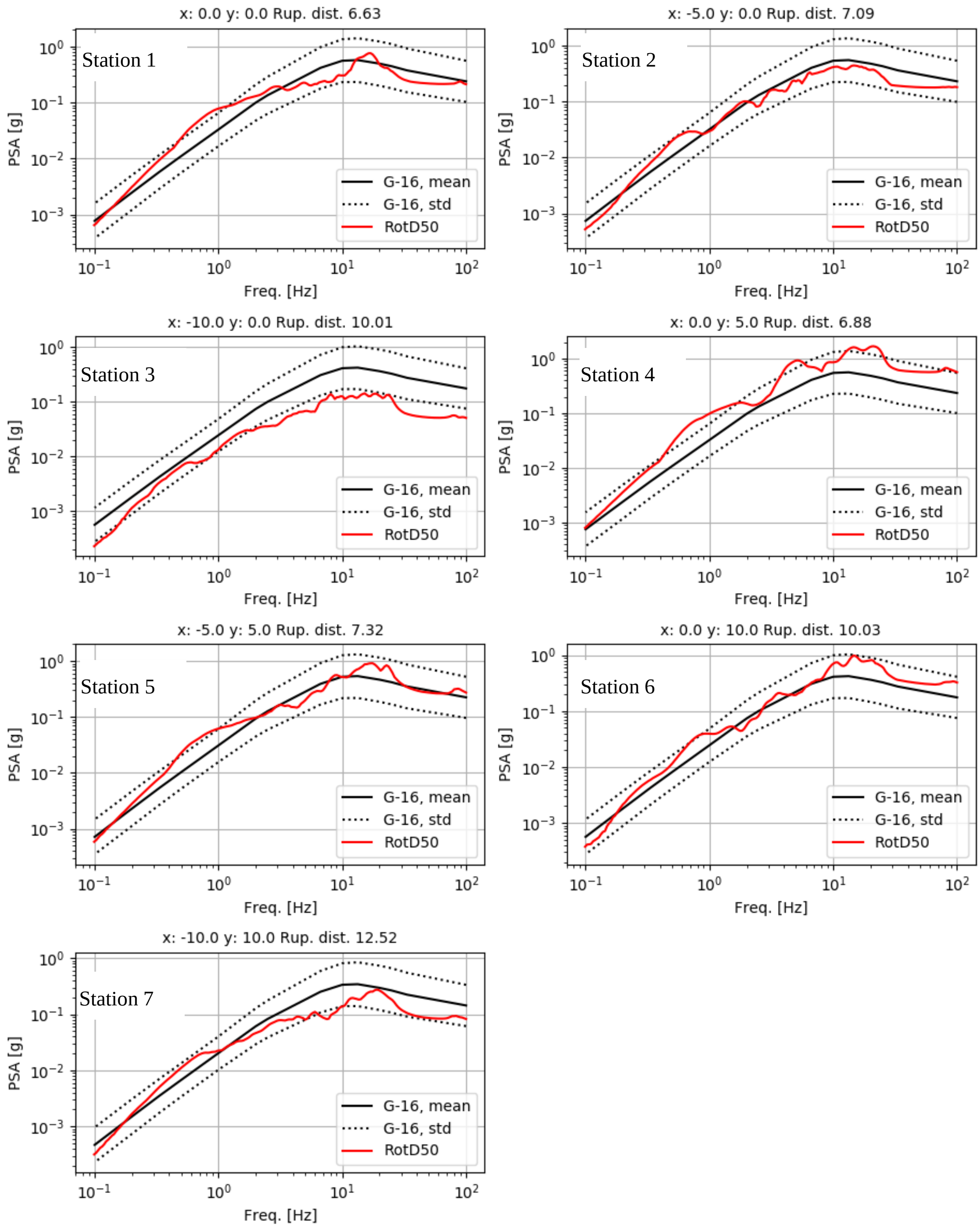

Figure 26. PSA spectra comparison between the G16 prediction and the Case #1 model outputs. Red lines are the model outputs (RotD50). Continuous black line is the mean prediction of G16, while dashed lines are the ± 1 standard deviation bounds predicted by G16. Station numbers refer to the ones given in Figure 11.

6 Conclusions

Within this report, we describe the modelling techniques and compare the modelling outcomes with ground motion prediction equations GMPEs developed for stable continental regions. By these comparisons we try to highlight the potentials and limitations of earthquake source modelling to support empirical observations.

Five cases were defined in order to explore the capabilities of ground motion simulation tool COMPSYN. In the five cases, the varied parameters were depth of the source, dip angle of the fault, focal mechanism and dynamic properties of the fault. COMPSYN and 3DEC simulations were compared in order to ensure correctness of the models. The assumed magnitude of the earthquake in the considered scenarios was M_w=5.5.

The results of the strike-slip simulation with homogenous fault properties i.e. Case #1 (Figure 14) shows wave propagation patterns similar to those presented by Stein and Wysession (2003). Similar wave propagation patterns can be found from the results of Case #3 and #4 (Figure 16 and Figure 17), since they are strike-slips as well. The differences compared to Case #1 are non-homogenous fault properties and shallower hypocentre for Case #3 and #4, respectively.

Cases #2 and #5 ground motion patterns (Figure 15 and Figure 18) are also reasonable for reverse slip movement in the north-south direction.

The major differences in strike and reverse slip faults are the ground motion in the epicenter and the amplitude of the displacements. The strike slip (Cases #1, #3 and #4) is almost silent in terms of displacement whereas reverse slip (Cases #2 and #5) have significant vertical ground motion in the epicenter. It should be noted as well that reverse slip resulted in general larger ground motion in terms of displacement within the considered distance of ~28km from the epicenter.

When it comes to comparing synthetic output to observation data, we opted to compare model outputs to existing GMPEs. In 2015 new Fennoscandian GMPEs were published, and the initial idea in this project was to compare the simulation results to these GMPEs. However, an inconsistency in the computation of the Fennoscandian GMPE has been identified, affecting especially the spectral shape produced by the new Fennoscandian GMPEs. Hence, we abandoned comparing modelling data to the Fennoscandian GMPEs, and we suggest that they should not be used for seismic hazard assessment before they are updated.

As alternative we decided to compare to the G16 GMPE developed for Central and Eastern North America by Graizer (2016). Since G16 was developed for hard rock sites in stable continental environments it can be regarded relevant as comparison to the COMPSYN simulation results.

The highest frequency relevant for the comparison was 25Hz, resulting from the limitations of the simulation results. The comparison of G16 and the COMPSYN simulation results spectra show reasonable overlap, except in the epicentre region.

We suggest further studies related to source modelling to improve NPP seismic safety in the Fennoscandian context. The short/medium term proposals are as follows:

- Making the simulation results more accurate, understanding where differences between model output and observations come from;
- Based on the encouraging results with regards to modelling, we suggest that it would be useful to use the modelling techniques developed in this project to generate a larger set of fault rupture scenarios and corresponding synthetic ground motion database for the near-field of M_w 5-6.5 earthquakes (where observations do not exist in Fennoscandia);

We also suggest further studies with relation to attenuation as follows:

- Updating the new Fennoscandian GMPEs to a standard procedure of calculating the geometric mean;
- Evolving the Fennoscandian GMPEs from the current geometric mean (GM) format to the more modern RotD50 or RotD100 format. This would reduce uncertainty of the hazard prediction, removing the randomness associated to recording direction. GM spectra can be affected by polarised recordings in the near-field. Since most hazards to the NPPs is generated by the near-field earthquakes it would be important to improve the representation of this distance range;

7 Acknowledgments

The authors wish to thank the NKS program for the opportunity to carry out this work as cooperation between Uppsala University, Aalto University, ÅF-Consult Oy, the Geological Survey of Denmark and Greenland, the University of Helsinki and VTT Technical Research Center of Finland Oy.

The authors also wish to acknowledge the support and helpful advice of Dr. Vladimir Graizer with the implementation of the G16 ground motion prediction equation.

The openness of Tommi Vuorinen to help decipher the calculation details of the two Fennoscandian GMPEs is also highly appreciated, especially considering the criticism we formulate in this study with reference to those GMPEs.

Dr. Pentti Varpasuo of PVA Engineeering Services provided useful suggestions when reviewing the initial results of the modelling reported. Those suggestions helped guide the interpretation of the model outcomes and improve the focus of our work.

NKS conveys its gratitude to all organizations and persons who by means of financial support or contributions in kind have made the work presented in this report possible.

8 Disclaimer

9 References

Bizzarri, A., 2012. Rupture speed and slip velocity: What can we learn from simulated earthquakes? Earth Planet. Sci. Lett. 317–318, 196–203. doi:10.1016/j.epsl.2011.11.023

Bizzarri, A., 2010. How to Promote Earthquake Ruptures: Different Nucleation Strategies in a Dynamic Model with Slip-Weakening Friction. Bull. Seismol. Soc. Am. 100, 923–940. doi:10.1785/0120090179

Bolt, B.A. (Ed.), 1987. Seismic strong motion synthetics, Computational techniques. Academic Press, Orlando, Fla.

Boore, D.M., 2010. Orientation-Independent, Nongeometric-Mean Measures of Seismic Intensity from Two Horizontal Components of Motion. Bull. Seismol. Soc. Am. 100, 1830–1835. doi:10.1785/0120090400

Boore, D.M., Watson-lamprey, J., Abrahamson, N.A., 2006. Orientation-independent measures of ground The 14th World Conference on Earthquake Engineering October 12-17. Bull. Seismol. Soc. Am. 1502–1511.

Cundall, P.A., 1971. A computer model for simulating progressive large scale movements in blocky rock systems, in: Symposium of the International Society for Rock Mechanics. Nancy, France.

Fälth, B., Hökmark, H., Lund, B., Mai, P.M., Roberts, R., Munier, R., 2015. Simulating Earthquake Rupture and Off-Fault Fracture Response: Application to the Safety Assessment of the Swedish Nuclear Waste Repository. Bull. Seismol. Soc. Am. 105, 134–151. doi:10.1785/0120140090

Fang, Z., Dunham, E.M., 2013. Additional shear resistance from fault roughness and stress levels on geometrically complex faults. J. Geophys. Res. Solid Earth 118, 3642–3654. doi:10.1002/jgrb.50262

Fülöp, L., Jussila, V., Lund, B., Fälth, B., Voss, P., Puttonen, J., Saari, J., 2016. Modelling as a tool to augment ground motion data in regions of diffuse seismicity - Progress 2015. NKS Nordic Nuclear Safety Research.

Gephart, J.W., Forsyth, D.W., 1984. An improved method for determining the regional stress tensor using earthquake focal mechanism data: Application to the San Fernando Earthquake Sequence. J. Geophys. Res. Solid Earth 89, 9305–9320. doi:10.1029/JB089iB11p09305

Gioncu, V., Mazzolani, F.M., 2011. Earthquake engineering for structural design. Spon Press, London ; New York.

Graizer, V., 2016. Ground-Motion Prediction Equations for Central and Eastern North America. Bull. Seismol. Soc. Am. 106, 1600–1612. doi:10.1785/0120150374

Ida, Y., 1972. Cohesive force across the tip of a longitudinal-shear crack and Griffith's specific surface energy. J. Geophys. Res. 77, 3796–3805. doi:10.1029/JB077i020p03796

Itasca, 2013. 3DEC – 3-Dimensional Distinct Element Code, User's Guide. Itasca Consulting Group Inc., Minneapolis, USA.

Jaeger, J.C., Cook, N.G.W., 1979. Fundamentals of rock mechanics, 3d ed. ed, Science paperbacks. Chapman and Hall ; distributed in U.S. by Halsted Press, London : New York.

Jussila, V., Fälth, B., Lund, B., Saari, J., Voss, P., Puttonen, J., Fülöp, L., 2017. Decreasing uncertainty in seismic hazard estimates in Fennoscandia by use of seismic source modeling. Ydintekniikka 46, 16–22.

Kanamori, H., Anderson, D.L., 1975. Theoretical basis of some empirical relations in seismology. Bull. Seismol. Soc. Am. 65, 1073–1095.

Kennedy, R.P., Short, S.A., Newmark, N.M., 1981. The response of a nuclear power plant to near-field moderate magnitude earthquakes.

Kottke, A.R., Rathje, E.M., 2009. Technical Manual for Strata (No. PEER 2008/10). Pacific Earthquake Engineering Research Center, 100.

Labbé, P., Altinyollar, A., 2011. Conclusions of an IAEA–JRC research project on the safety significance of near-field seismic motions. Nucl. Eng. Des., ICONE-17: Heavy Liquid Metal Technologies and Material Challenges for Gen IV Fast Reactors 241, 1842–1856. doi:10.1016/j.nucengdes.2011.02.006

Leonard, M., 2010. Earthquake Fault Scaling: Self-Consistent Relating of Rupture Length, Width, Average Displacement, and Moment Release. Bull. Seismol. Soc. Am. 100, 1971–1988. doi:10.1785/0120090189

Malm, M., Saari, J., 2014. SESA, Subproject 1 - Earthquake Hazard Assessment, Progress Report 2014 (Research Report No. DSAF14R). ÅF-Consult Ltd.

Mentrasti, L., 2008. Estimate of spectral and pseudo-spectral acceleration proximity. Eng. Struct. 30, 2338–2346. doi:10.1016/j.engstruct.2008.01.002

Olson, A.H., Orcutt, J.A., Frazier, G.A., 1984. The discrete wavenumber/finite element method for synthetic seismograms. Geophys. J. Int. 77, 421–460. doi:10.1111/j.1365-246X.1984.tb01942.x

Pezeshk, S., Zandieh, A., Tavakoli, B., 2011. Hybrid Empirical Ground-Motion Prediction Equations for Eastern North America Using NGA Models and Updated Seismological Parameters. Bull. Seismol. Soc. Am. 101, 1859–1870. doi:10.1785/0120100144

Spudich, Paul, Xu, L., 2003. 85.14 Software for calculating earthquake ground motions from finite faults in vertically varying media, in: William H.K. Lee, H.K., Paul C. Jennings and Carl Kisslinger (Ed.), International Geophysics, International Handbook of Earthquake and Engineering Seismology. Academic Press, pp. 1633–1634.

Spudich, P, Xu, L., 2003. Documentation of software package ISOSYN v3.11: Isochrone integration programs for earthquake ground motion calculation, in: CD3 Accompanying the International Handbook of Earthquake and Engineering Seismology.

Stein, S., Wysession, M., 2003. An introduction to seismology, earthquakes, and earth structure. Blackwell Pub, Malden, MA.

SWISSNUCLEAR, 2004a. Probabilistic Seimic Hazard Analysis for Swiss Nuclear Power Plant Sites (PEGASOS project): Final Report Volume 2 - Results (Final Report). Wettingen.

SWISSNUCLEAR, 2004b. Probabilistic Seimic Hazard Analysis for Swiss Nuclear Power Plant Sites (PEGASOS project): Final Report Volume 4 - Elicitation summaries, Seismic Source characterization (Final Report). Wettingen.

Toro, G., 2002. Modification of the Toro et al.(1997) attenuation equations for large magnitudes and short distances. Risk Engineering, Inc.

Vuorinen, T., 2015. New Fennoscandian Ground Motion Characterization Models (MSc thesis). University of Helsinki, Helsinki, Finland.

YVL B.7, 2013. Provisions for internal and external hazards at a nuclear facility, Finnish Regulatory Guide on Nuclear Safety (YVL).

Zoback, M.D., Townend, J., 2001. Implications of hydrostatic pore pressures and high crustal strength for the deformation of intraplate lithosphere. Tectonophysics 336, 19–30. doi:10.1016/S0040-1951(01)00091-9

Bibliographic Data Sheet **NKS-394**

Title	Modelling as a Tool to Augment Ground Motion Data in Regions of Diffuse Seismicity – Final report
Author(s)	Ludovic Fülöp[1], Vilho Jussila[1], Björn Lund[2], Billy Fälth[2], Peter Voss[3], Jari Puttonen[4], Jouni Saari[5], Pekka Heikkinen[6]
Affiliation(s)	[1]VTT Technical research Centre in Finland Oy, [2]Uppsala University, [3]Geological Survey of Denmark and Greenland, [4]Aalto University, [5]ÅF Consult Oy, [6]Institute of Seismology, University of Helsinki
ISBN	978-87-7893-482-6
Date	August 2017
Project	NKS-R / AddGROUND
No. of pages	44
No. of tables	4
No. of illustrations	26
No. of references	33
Abstract max. 2000 characters	De-aggregation of probabilistic hazard assessment (PSHA) results show that the dominating source of vibrations with engineering significance to NPP safety is from mid-magnitude earthquakes located at close distances to the plant. This region is called the "near-field" and is known for its particularities when compared to "far-field". For example, significant duration of the ground motions is shorter, corresponding to S-wave and surface wave arrivals; there are distinctive high velocity peaks in the ground motions and vertical

shaking components may exceed horizontal components. These particularities are known to have design consequences, but are often overlooked by engineering codes.

In Fennoscandia, near-field observations of larger magnitude ($M>3$) earthquakes are missing, and modelling is the only way to supplement the existing empirical data underspinning the attenuation equations in the PSHA studies.

During the project year 2015, we confirmed the near-source effect in small magnitude earthquake recordings in Finland and developed modeling skills and tools to generate synthetic, near-field accelerograms starting from process of the fault rupture.

Within this report (2016), we describe the modelling techniques and compare the modelling outcomes for Mw=5.5 earthequakes with ground motion prediction equations GMPE’s developed for stable continental regions. Five cases were analyzed in order to explore the capabilities of ground motion simulation tools. In the five cases, the varied parameters were depth of the source, dip angle of the fault and dynamic properties of the fault. The models were developed in COMPSYN in 3DEC.

By these comparisons we highlight the potentials and limitations of modelling to support empirical observations.

Key words

Nuclear power plant safety, earthquake, near-field effects, fault source modeling